Experimental Investigation and Numerical Simulation of Cs-based Vacancy-Ordered Double Perovskites for Solar Cell Development

By

Akfeen Amjad

Department of Chemistry

Quaid-i-Azam University

Islamabad Pakistan

2023

Experimental Investigation and Numerical Simulation of Cs-based Vacancy-Ordered Double Perovskites for Solar Cell Development

وَمَن يُؤْتَ الْحِكْمَةَ
فَقَدْ اُوتِيَ خَيْرًا كَثِيرًا

QUAID-I-AZAM UNIVERSITY

ISLAMABAD

A dissertation submitted to the Department of Chemistry,

Quaid-i-Azam University, Islamabad, in partial fulfilment of the

requirement for the degree of

Master of Philosophy

in

Inorganic/Analytical Chemistry

by

Akfeen Amjad

Department of Chemistry,

Quaid-i-Azam University, Islamabad, Pakistan,

2023

بِسْمِ اللهِ الرَّحْمٰنِ الرَّحِيمِ

This is to certify that this dissertation entitled **"Experimental Investigation and Numerical Simulation of Cs-based Vacancy-Ordered Double Perovskites for Solar Cell Development"** submitted by *Ms. Akfeen Amjad* is accepted in its present form by the Department of Chemistry, Quaid-i-Azam University, Islamabad, as satisfying the dissertation requirements for the degree of Master of Philosophy in *Analytical/Inorganic Chemistry*.

External Examiner:

M. Saif Khan.

Dr. Muhammad Saifullah Khan
Principal Scientist
Chemistry Division
Pakistan Atomic Energy Commission
P.O. Box 1611, Islamabad.

Supervisor & Head of Section:

Zareen Akhter

Prof. Dr. Mrs. Zareen Akhter
Department of Chemistry
Quaid-i-Azam University
Islamabad

Chairman:

Prof. Dr. Aamer Saeed Bhatti
Department of Chemistry
Quaid-i-Azam University
Islamabad

Author declaration

I hereby declare that all the experimental work was performed originally by me in the Inorganic Chemistry Laboratory, Department of Chemistry, Quaid-i-Azam University, Islamabad, Pakistan. To the best of my knowledge, this work is original and has never been presented by any other person or for any other degree on any other platform.

Akfeen Amjad

Dedication

With love and respect, this thesis is dedicated to,

my beloved parents,

AMJAD HUSSAIN
AND
ABIDA AMJAD

Acknowledgments

Abstract

Vacancy-ordered perovskites (VOPs) represent a promising class of materials that offer lead-free alternatives with tunable properties, enhanced stability, and potential applications in solar cells, LEDs, sensors, and more. This study focuses on synthesizing and characterizing vacancy-ordered $Cs_2SnI_{6-x}Br_x$ perovskite films at different temperatures (100 °C, 120 °C and 140 °C). The starting materials were first synthesized and characterized through XRD analysis. The films were then synthesized, using these materials at varying temperatures in a closed reactor, and were analyzed through XRD, DRS, Hall measurements, SEM, and EDX analysis. The objective was to comprehend the impact of synthesis temperature on perovskite films. These findings enhance the understanding of structural evolution in the films, offering pathways to tailor their properties for solar cell applications. Furthermore, utilizing SCAPS-1D software, the study optimized an environmentally friendly, lead-free vacancy-ordered Cs_2PtI_6 solar cell with MoO_3 as the hole transport layer (HTL) and $Sr^\curvearrowright$ as the electron transport layer (ETL). Further, effect of varying absorber layer, HTL and ETL thicknesses, absorber and interface layer defect density, effect of operating temperature, work function of back contact, series and shunt resistance of device parameters were studied. Quantum efficiency studies on the device were also carried out. This study highlights the importance of optimization of these parameters in achieving high-performance solar cells.

Table of Contents

List of Figures

List of Tables

List of Abbreviations

AMPS	Analysis of microelectronic and photonic structure
CB	Conduction band
CBM	Conduction band minima
CIGS	Copper indium gallium selenide
DRS	Diffused reflectance spectroscopy
DSSCs	Dye sensitized solar cells
EDX	Energy dispersive X-ray
ETL	Electron transport layer
FA	Formamidinium
FF	Fill factor
FTO	Fluorine doped tin oxide
GO	Graphene oxide
GaAs	Gallium arsenide
HOMO	Highest occupied molecular orbital
HPSCs	Hybrid perovskite solar cells
HTL	Hole transport layer
IGZO	Indium gallium zinc oxide
I-V	Current-voltage
I_{sc}	Short circuit current
J_{sc}	Short circuit current density
J-V	Current density-voltage
LEDs	Light emitting diodes
LUMO	Lowest unoccupied molecular orbital
MA	Methylammonium
N_t	Defect density
PCE	Power conversion efficiency
PCBM	Phenyl-C61-butyric acid methyl ester
PSCs	Perovskite solar cells
QE	Quantum efficiency
R_s	Series resistance
R_{sh}	Shunt resistance
SCAPS-1D	Solar cell capacitance simulator in 1 dimension

SEM	Scanning electron microscopy
VB	Valence band
VBM	Valence band maxima
V_{oc}	Open circuit voltage
VOPs	Vacancy ordered perovskites
XRD	X-ray diffraction

Chapter 1

Introduction

1.1 Global energy demand and renewable energy

The 21st century has witnessed an exponential surge in worldwide energy consumption, mainly influenced by population growth, urbanization, and the widespread assimilation of technology into daily life. This phenomenon has led to a critical juncture in the energy landscape of world, marked by an imminent energy crisis. Traditional fossil fuels, including coal, oil, and natural gas, have been the backbone of world energy production for decades. However, their excessive utilization has not only strained their availability but has also caused environmental challenges such as air pollution and climate change. As a response to these challenges, renewable energy sources have emerged as a beacon of hope, offering a pathway to alleviate the energy crisis while ensuring long-term environmental sustainability[1].

Renewable energy sources encompass solar, geothermal, wind, biomass and hydroelectric energy. They are eco-friendly, emitting minimal greenhouse gases, thus aiding in climate change mitigation. Solar energy, harnessed through photovoltaic cells, provides a promising solution, particularly in high sunlight zones. Wind energy capitalizes on the kinetic energy of moving air masses, while hydroelectric power is derived from flowing water. Geothermal energy taps into the internal heat of Earth, while biomass energy uses organic matter to generate fuel. These sources collectively present a multifaceted approach to combating the energy crisis[2].

1.1.2 Solar power

Solar energy holds significant potential as a power source to lower carbon emissions. The solar energy that falls on all of the continents is more than 200 times greater than the annual total commercial power currently consumed by humans[3]. Solar energy can be produced simply by using photovoltaic cells, which are made of semiconductors and can store energy in batteries for further use in various operations.

For a considerable time, crystalline silicon has dominated the solar sector. Even though other alternatives like thin-film solar cells have emerged, they hold only a modest 5 % market share. This is due to the intricate challenge of matching the efficiency and cost-effectiveness of traditional silicon cells. But there are also problems

associated with silicon cells, such as high cost and an efficiency limit of 22 %. Manufacturing silicon panels is complex due to the high heat needed to remove impurities. To overcome these limits, new alternatives are being searched. Within the last few years, there has been a significant rise in interest mainly in the use of organic–inorganic hybrid perovskite materials for solar cell applications, due to its high-power conversion efficiency (PCE) and simple and cost-effective production[4-11]. Since 2009, its efficiency has increased from 3.8 % to 25.8 %, over a mere decade, exceeding the earlier records of 23.4 % for $Cu(In,Ga)Se_2$, 22.8 % for multi-crystalline silicon solar cells and 22.1 % for CdTe. However, there are still several concerns to be addressed that retard the practical applicability of these halide perovskite, majorly including toxicity of lead and air/moisture instability[12-17].

1.2 Generation of solar cells

Solar photovoltaic technology can be categorized into four generations of solar cells, each based on their manufacturing processes. The first generation comprises diverse crystalline silicon solar cells, with single-crystalline variants achieving efficiency levels between 18 % and 25.6 %, while multi-crystalline versions exhibit efficiencies within the range of 17 % to 20.8 %. Silicon is the most common semiconducting element used in solar cells. The second-generation contain thin-film solar cells whose efficiency varies based upon the type of material used. For instance, thin-film solar cells utilizing CdTe exhibit efficiencies ranging from 18.3 % to 22.1 %. Amorphous silicon cells achieve an efficiency of 13.4 %, while solar cells utilizing copper indium gallium selenide showcase efficiencies between 20.4 % and 22.6 %.

The third generation consists of dye-sensitized solar cells (DSSCs), perovskite solar cells (PSCs)[18-20], organic solar cells and multi-junction solar cells. Organic solar cells are composed primarily of carbon-rich organic compounds. These compounds are of critical importance in the manipulation of the band gap, alteration of transparency, and manipulation of the colour of the light-active material. For multi-junction solar cells, the highest efficiency recorded is about 45 %.

The fourth generation encompasses emerging solar cell technologies, including inorganic hybrid and heterojunction solar cells. Ongoing efforts are directed towards enhancing the efficiency of these solar cells[21]. **Fig 1.1** shows the advancements in solar cell efficiency over time.
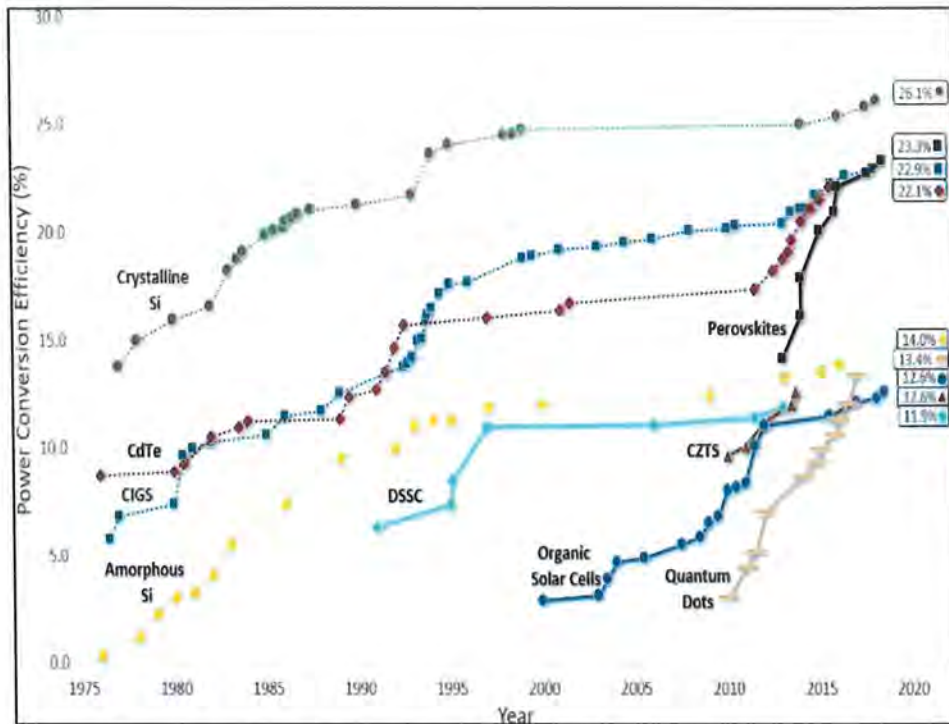
Figure 1.1: Advancements in solar cell efficiency over time[21]

1.3 Perovskite materials

1.3.1 Crystal structure of perovskite

Perovskite material comprises solid structures formed by combining metals (A and B cations) and non-metals (X anions, mainly halogens) in a specific atomic arrangement. The most common form of perovskite is calcium titanate. Its structure is denoted by the formula ABX_3, where A represents large organic cations like cesium, rubidium, formamidinium $(CH(NH_2)_2^+)$, or methylammonium $(CH_3NH_3^+)$; B denotes divalent cations like Sn^{2+}, Pb^{2+}, Mn^{2+}, Ge^{2+} *etc.* and X indicates monovalent anions I^-, Br^-, Cl^-. The larger A cation coordinates with twelve X anions, while the smaller B cation is in the middle of the cube at an octahedral site with six X ions located at the face of the cube as shown in **Fig 1.2**. The hybrid halide perovskite $(CH_3NH_3PbI_3/FAPbI_3)$, in general, exhibits an intricate structural profile characterized by successive transitions among cubic, tetragonal, and orthorhombic polymorphs, around the temperature range of 165 K to 327 K[22].

3

A Site= Cs $^{+1}$, Rb^{+1} Organic A Site=(FA^{+1}, MA^{+1})
B Site= Sn^{2+}·Ge^{2+}·Pb^{2+}· Mn^{2+}·Cd^{2+}
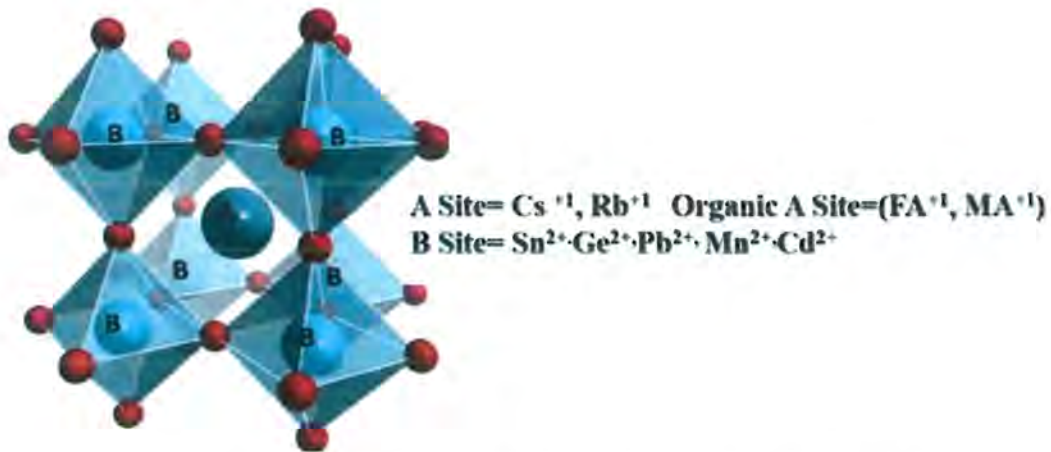
Figure 1.2: Cubic crystal structure of perovskite ABX$_3$ [22]

Some of these perovskite structures are homo-valent (II) to lead-based perovskite and some are hetero-valent, providing vast combinatorial chemistry options because of the broad variety of possibilities for different B-site cations. In theory, a diverse range of compounds could conform to the chemical formula ABX$_3$, although not all are crystallographically stable.

1.3.2 Problems associated with lead-halide perovskites

1.3.2.1 Degradation and toxicity issues

In recent times, there has been an increasing interest in hybrid perovskite solar cells (HPSCs) due to their remarkable intrinsic traits, including lower production costs, higher carrier mobilities, tunable band gaps, long carrier diffusion lengths, and high absorption coefficient[6-7,19,22-25]. In just over a decade, the PCE has dramatically increased from 3.3 % to 25.7 % due to the synergistic optimization of device interfaces. Full industrialization of HPSCs, in spite of having achieved an efficiency of over 25 % is trammelled by two main issues: Pb toxicity and instability. Lead halide perovskites, upon exposure to oxygen, light, heat, and moisture, degrade through various pathways[12-17].

Organic ions, methylammonium (MA$^+$) and formamidinium (FA$^+$) at the 'A' site of perovskite are unstable and degrade in atmospheric operational conditions. Notably, methylammonium lead triiodide (MAPbI$_3$), dissolves into MAI and PbI$_2$ under humid conditions. Furthermore, the MAPbI$_3$ perovskite cannot resist high temperatures (140 °C) and can be degraded into PbI$_2$ even at temperatures of 85 °C for an extended period of time, which is closely associated with the volatile organic molecule MA^{+13}.

In addition to stability issues, toxicity of lead is also a critical issue. Its proclivity to bond with enzymes, proteins, and cell membranes poses carcinogenic risks and endangers vital organs such as the kidneys, brain, central nervous system, and liver. Poisoning from it can cause irreversible health problems in children and pregnant women[26-27]. Thus, even with their comprehensive attributes, organic Pb-based PSCs encounter constrained practicality. So, it has become necessary to investigate lead-free perovskite materials that provide improved stability and PCEs without endangering human health or the environment.

1.3.2.2 Possible solutions; lead-free all inorganic double perovskites

Finding stable, non-toxic, and highly efficient perovskites has proven to be an enormous problem to date. Substituting organic components (MA^+, FA^+) with the inorganic Cs^+ has significantly mitigated thermal degradation and volatilization issue in hybrid perovskite by enhancing crystal structure stability. Similarly, with the imperative to mitigate toxicity of lead, researchers are increasingly replacing Pb^{+2} with metals like Te, Sn, Zr, Ti, Au, and Pt, advancing the field towards all-inorganic, lead-free perovskite as the forefront solution[28].

In recent years, vacancy-ordered halide double perovskites, A_2BX_6 (A = Cs, Rb; B = Te, Sn, Pt, Ti, Zr; X = I, Br and Cl) have gained prominence as non-toxic and stable substituents for their lead-based counterparts in optoelectronic applications. These lead-free double perovskites have good stability, narrow direct band gaps, high carrier mobility, high optical absorption coefficients, and good charge transport properties[29], making them viable candidates for future solar cell applications.

1.4 Double perovskites (vacancy-ordered perovskites)

1.4.1 Crystal structure and properties

Among heterovalent Pb-free perovskite structures, double perovskites have surfaced as a stable, environmentally friendly alternative to lead halide perovskites. Double perovskites exhibit a unit cell twice the size of the traditional perovskite (hence the name 'double perovskite'). Their general formula is $A_2B_2X_6$ or $A_2BB'X_6$, where A denotes an alkaline metal, B and B′ are transition metals, while X represents halides or mixed halides. Within the realm of double perovskites, unmixed forms with the A_2BX_6 structure are commonly termed vacancy-ordered perovskites (VOPs)[30-31]. These entities

are characterized as defect-ordered derivations of the perovskite crystalline structure, exhibiting an antifluorite configuration where individual octahedral units are interconnected through A-site cations as shown in **Fig 1.3**.

(a)

ABX_3 x2 → $A_2B_2X_6$ −B → A_2BX_6

(b) A_2MX_6

A^{+1} M^{+4} X^{-1}
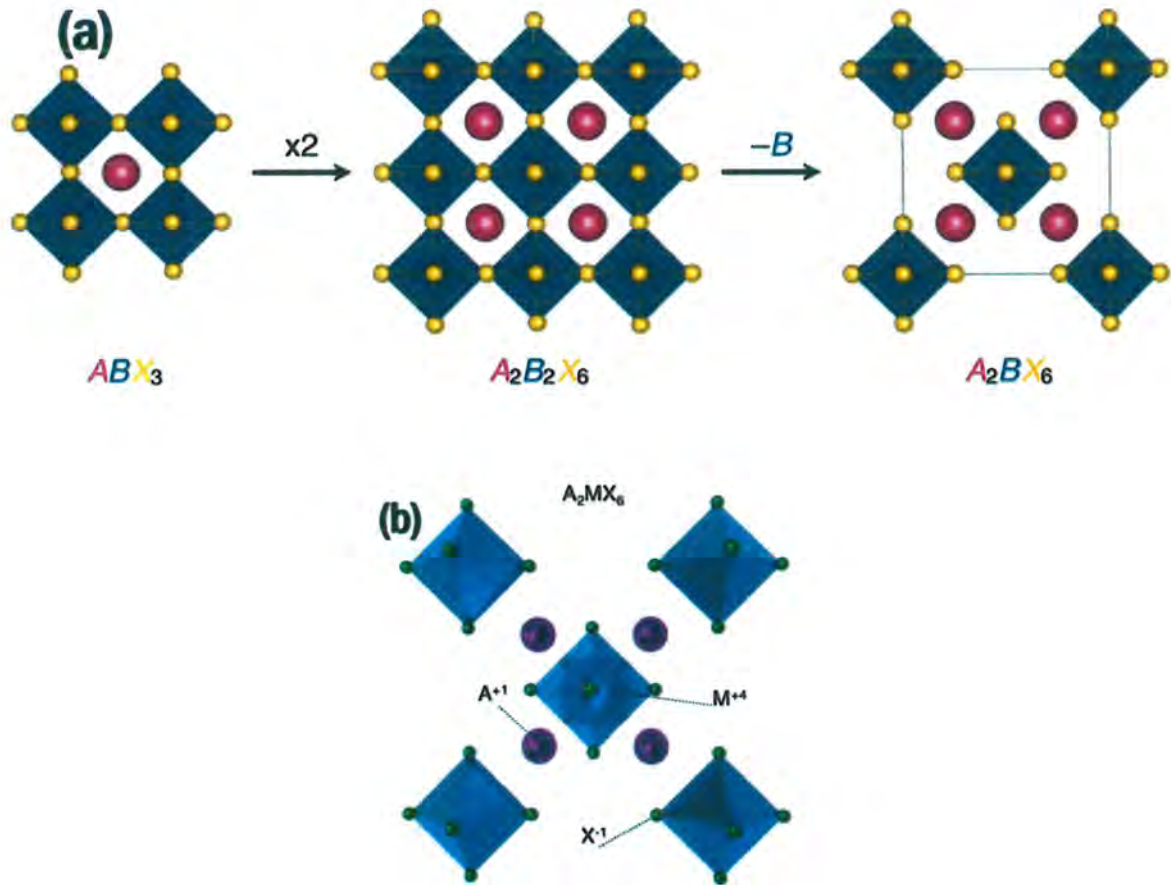
Figure 1.3: *(a) Representation of double perovskite derivation from* ABX_3[30] *(b)* A_2BX_6 *crystal structure*[31]

In vacancy-ordered double perovskites, $A_2M(IV)X_6$, Pb (II) ions are replaced by M^{+4} tetravalent ions and a vacancy site "□" to maintain charge balance similar to those found in (ABX_3) perovskites. The cubic configuration (Fm3m) of these double perovskite compounds, coupled with their capability to expand three-dimensionally through shared metal halide octahedra, has stimulated extensive attention towards their use as efficient optoelectronic candidates.

VOPs are viable alternatives for substitution because they have minimal toxicity, high optical absorption coefficients, narrow direct bandgaps, excellent carrier mobility, and effective charge transport properties, and could be used as photocatalysts, X-ray detectors, photodetectors, lasers, LEDs and solar cells [31-36].

1.5 Use of cesium tin (IV) halide (Cs$_2$SnX$_6$) perovskite in solar cells

Tin is regarded as the best metal cation used in place of lead for better stability of inorganic halide perovskites. Because of the narrow bandgap, high carrier mobility, low exciton binding energy, and long diffusion length, tin based perovskites are regarded as a prime contender for light-harvesting material in optoelectronic applications. Therefore, progress has been made on tin-based perovskite for the past few years. The main reasons to synthesize tin-based perovskites are low-temperature fabrication, suppressed behaviour of hysteresis, and cost-effectiveness[8,37-39]. **Fig 1.4** shows the crystal structure of cesium tin halide double perovskite.
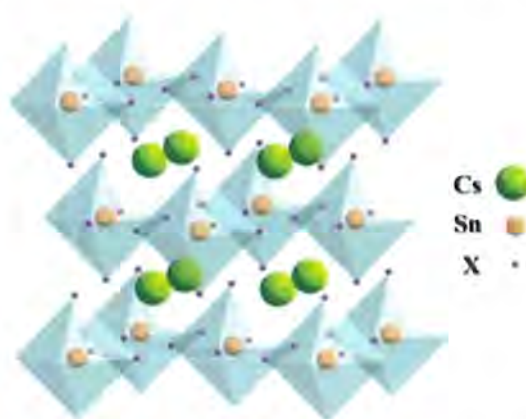
Figure 1.4: Crystal structure of Cs$_2$SnX$_6$[39]

Cs$_2$SnI$_6$, the first inorganic defect variant perovskite material, with tin in +4 oxidation state, having an inbuilt resistance to oxidation, has received a lot of attention[38]. It exhibits a direct band gap of 1.30 – 1.62 eV, implying a theoretical Shockley-Queisser efficiency of 30 – 33 %. Limited research has been done on the synergistic optimization of the cesium tin perovskite and Cs$_2$SnI$_6$ still remains a seldom explored material. **Table 1.1** summarizes the use of Cs$_2$SnX$_6$ in solar cells so far.

Table 1.1: Use of Cs$_2$SnX$_6$ in solar cells

Year	Material	Work	Reference
2014	Cs$_2$SnI$_6$	As HTL in dye sensitized solar cells (DSSCs)	40
2016	Cs$_2$SnI$_6$	As ETL	41
2016	Cs$_2$SnX$_6$ (X= Cl, Br, I))	Perovskite Solar Cell	42
2016	Cs$_2$SnI$_6$	Stress Test on DSSCs	43
2017	Cs$_2$SnI$_6$	Modifier in DSSCs	44

2020	Cs_2SnI_6	As HTL in DSSCs	[45]
2022	Cs_2SnX_6 (X= Br, I)	Dye sensitized solar cell	[46]
2022	Cs_2SnI_6	Dye sensitized solar cell	[34]
2022	Cs_2SnI_6 nanocrystals	Carbon based $CsPbI_2Br$ PSCs	[47]

The Cs_2SnI_6 films can be made via spray-coating/electro-spraying, vacuum thermal deposition or vapor assisted deposition; aerosol-assisted chemical vapor deposition[48-49]. To further improve the bandgap, gain stability and improve conductivity, bromine could be incorporated in Cs_2SnI_6 to make $Cs_2SnI_{6-x}Br_x$[46].

1.6 Use of cesium platinum (IV) iodide (Cs_2PtI_6) perovskite in solar cells

Cs_2PtI_6 is one of the intriguing materials in the A_2BX_6 class. Its crystal structure is shown in **Fig 1.5**. Cs_2PtI_6 is an ideal option for PSCs due to its higher carrier mobility, higher absorption coefficient ($4 \times 10^5 \, cm^{-1}$), narrow band gap (1.37 eV), and dynamically stable structure[50]. With a tolerance factor of 0.97, it is able to have a highly consistent cubic structure, hence increasing its stability. It is stable under harsh conditions, including high temperatures, UV light, and high humidity[51]. It could serve as an appropriate substitute for perovskite-containing lead due to its oxidation resistance, high atomic number, and stability beyond non-toxicity. Cs_2PtI_6 is a highly advantageous photovoltaic material due to all of these qualities.

Pt^{4+} I^- Cs^+
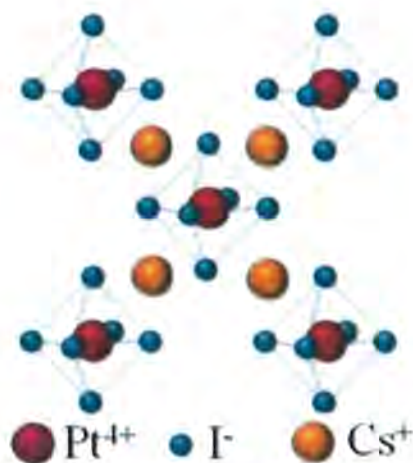
Figure 1.5: Crystal structure of Cs_2PtI_6[52]

Unfortunately, systematic simulation and device modelling for the properties of Cs_2PtI_6, which are essential for their optoelectronic devices, are seldom investigated,

resulting in subpar efficiency. To optimize and boost the performance of Cs_2PtI_6-based PSCs, it is required to construct a band structure that minimizes charge recombination while enhancing carrier separation and transport. For this objective, device simulation is used to attain a thorough comprehension of how material properties relate to performance parameters. **Table 1.2** summarizes the use of Cs_2PtI_6 in perovskite solar cells.

1.7 Working principle of solar cells

Solar cells generate electricity based on the photovoltaic effect. This effect involves the conversion of light energy into electrical energy. The solar-to-electrical energy conversion efficiency of solar cells is highly dependent on their design and composition. A photovoltaic device requires three fundamental parts: a cathode, an anode, and a photoactive layer. **Fig 1.6** shows the general representation of a p-n junction solar cell. Sunlight (photons) hits the cell surface, and the absorber material absorbs the photons. Photon energy excites electrons in the absorber layer, creating electron-hole pairs. This leads to a voltage difference across the cell, causing electrons to move to the n-type layer and holes to the p-type layer. An external circuit completes, and electrons flow, generating electric current. Metal contacts collect the current for external use.
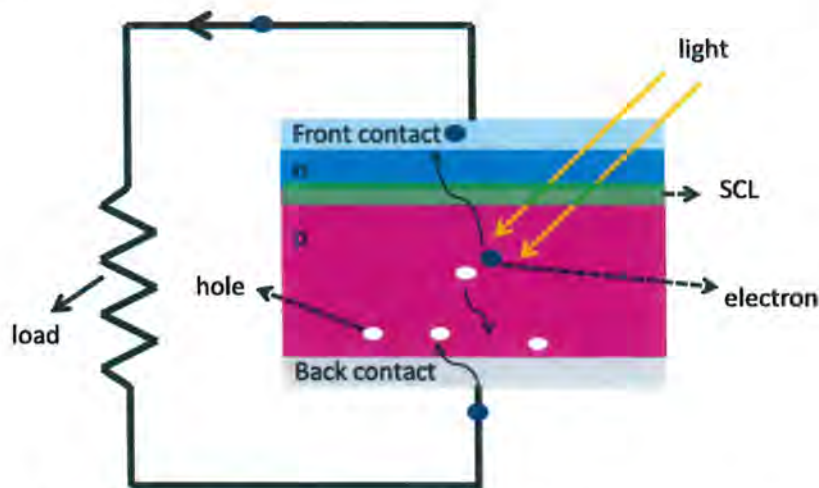
Figure 1.6: General representation of a p-n junction solar cell[55]

To mitigate charge recombination and enhance charge collection, electron/hole transport materials are often modified in electronic devices. In the majority of electronic devices, electron/hole transport materials can be modified to prevent charge recombination and enhance charge collection.

9

Table 1.2: *Use of Cs$_2$PtI$_6$ in perovskite solar cells (PSCs)*

Device Architecture	V$_{oc}$ (V)	J$_{sc}$ (mA/cm^2)	FF (%)	PCE (%)	Experimental / Simulation	Reference
ITO/SnO$_2$/Cs$_2$PtI$_6$/ Spiro-OMeTAD /Au	0.73	1.20	82.00	0.72	Experimental	50
FTO/ CdS/ Cs$_2$PtI$_6$ with EDA/carbon/Cu	1.07	19.84	65.03	13.88	Experimental	51
FTO/CdS/Cs$_2$PtI$_6$/ Carbon/Cu	1.20	20.20	41.51	10.06	Experimental	51
FTO/ZnO/Cs$_2$PtI$_6$/ MoO$_3$/Cu	1.38	16.1070	75.54	16.85	Simulation	53
FTO/ZnO/Cs2PtI6/ MoO$_3$/C	1.41	16.1122	90.01	20.45	Simulation	53
FTO/CdS/Cs$_2$PtI$_6$/ MoO$_3$/Cu	1.11	20.14	61	13.9	Simulation	54
FTO/CdS/ Cs$_2$PtI$_6$/ Cu$_2$O /Cu	1.10	20.4	62	14.2	Simulation	54
FTO/CdS/Cs$_2$PtI$_6$/ CuI /Cu	1.12	20.13	60	13.7	Simulation	54
FTO/IGZO/Cs$_2$PtI$_6$/ Cu$_2$O/C	1.13	22.2	59.2	14.8	Simulation	54
FTO/ZnSe/Cs$_2$PtI$_6$/ Cu$_2$O/C	1.12	22.3	58	14.7	Simulation	54
FTO/WS$_2$/Cs$_2$PtI$_6$/ Cu$_2$O/C	1.10	28.1	52.4	16.3	Simulation	54

1.8 Perovskite solar cells

Perovskite solar cells are one of the most extensively studied topic of third-generation photovoltaics because of the rapid rise in power conversion from 3.8 % in

2009 to 25.8 % in 2021. In typical PSCs, the photoactive perovskite material is sandwiched between two charge transport layers[56-59].

1.8.1 Layers of perovskite solar cells (PSCs)

1.8.1.1 Absorber layer

In perovskite solar cells, the absorber layer plays a pivotal role as the primary light-absorbing component. This layer possesses key attributes such as a high absorption coefficient, a longer diffusion length, and a low exciton binding energy. Perovskite solar cells comprise a thin light-harvesting absorber (perovskite) layer, provided by an n-type electron transport layer (ETL) and a p-type hole transport layer (HTL). These layers simultaneously act as barriers for opposite charge carriers. Here, the alignment is necessary for the energy bands. The conduction band of the ETL must reside below the perovskite layer, while the valence band of the HTL must reside above it. Maintaining a suitable energy gap between these bands enhances contact differences. The nature of the absorber layer depends on the A cation, which can be organic or inorganic. Inorganic cations like cesium are thermally stable, motivating the substitution of organic cations with inorganic cations.

1.8.1.2 Selective contacts

In perovskite solar cells, charge separation and transportation occurs at the interfaces of the perovskite/electron transport layer (ETL) interface and the perovskite/hole transport layer (HTL) interface. The primary role of ETL is to extract light-generated electrons from the perovskite layer and transport them to the cathode. Conversely, the HTL facilitates the transportation and removal of holes. The selection of ETL and HTL materials depends on factors such as current-voltage parameters, stability, and recombination at the interfaces. Commonly employed charge transport layers in perovskite solar cells include NiO, SnO_2, ZnO, PCBM, C_{60}, MoO_3, CuI, Spiro-OMETAD, and TiO_2[60].

1.8.1.3 Electrode materials

The electrode layer, positioned at the top and in direct contact with the environment, holds pivotal significance for solar cell performance. The electrode must have the characteristics to overcome the diffusion of moisture and do not encounter any kind of reaction chemically. For example, Ag, Au, and Cu electrodes are most commonly employed electrodes in PSCs[61].

1.8.2 Working of perovskite solar cells

The working principle of PSCs is like other solar cells as shown in **Fig 1.7**. The perovskite solar cell operates on the following steps:

- Production of free charge carriers by the light absorbed in the perovskite layer
- Transportation of free charge carriers by the process of diffusion
- Movement of charge carriers to their respective transport layers and then to the electrodes[60].

Various undesirable processes take place in the perovskite solar cells. These are ion recombination, direct contact between HTL and ETL and transfer of back charges at the perovskite/HTL interface and perovskite/ETL interface. After dealing with such undesirable processes, the remaining charge carriers are carried out at the electrodes with the help of selective contacts. There are three main reasons responsible for the unnecessary charge recombination in PSCs:

- Direct contact of ETL and HTL through the shunt paths
- Within the bulk perovskite film, recombination takes place
- Recombination at the perovskite/HTL or perovskite/ETL interface[62]

Figure 1.7: *The schematic working principle of a perovskite solar cell*[63]

Minimizing parasitic losses in a perovskite solar cell requires ensuring compatibility among all layers and layer interfaces. This compatibility is crucial for achieving high power conversion efficiency. Factors such as carrier mobility, energy barriers, band gap alignment, and interfacial vacancies play an important role in determining compatibility, affecting cell performance and stability. Therefore, the

design of suitable cell interfaces is paramount for both short-term cell success and long-term stability, a crucial aspect for potential commercialization.

1.9 Simulation theory background (overview of SCAPS-1D)

Device modelling deals with major approach to gain a detailed conception for the physical functioning, the practically proposed explanations and the improvements of physical modifications upon conductivity of photovoltaic cells. Synthesizing a solar cell device without theoretical modelling is not feasible as well as a waste of time. It not only reduces danger, saves money and time, but it also examines the characteristics of different layers, as a result which improves the conductivity of a photovoltaic cell. Different softwares have been used for modelling of photovoltaic cell devices *i.e.,* SCAPS-1D, AMPS, and SILVACO *etc.*[64].

SCAPS-1D is a solar cell capacitance simulator in one dimension. The main characteristics of SCAPS, such as different input parameters of matter also their defect properties could get specified in seven semiconducting layers[53]. Different parameters such as absorber layer defect density, interface layer defect density, shunt and series resistance, working temperature, concentration gradient of layers used, all could be varied to obtain an optimized device configuration. One can analyse J-V characteristics, device efficiency (η), open circuit voltage (V_{oc}), fill factor (FF), short circuit current density (J_{sc}), spectral response (QE) of device using SCAPS-1D. Initially this software was used for the second generation (polycrystalline crystal) like $CuInSe_2$ and CdTe. Over time, this program has been developed to include more mechanisms *i.e.,* this software is used for crystalline solar cells (Si and GaAs) and amorphous solar cells (a-Si), and perovskite solar cells[65].

Recent research has focused on the SCAPS analysis of vacancy-ordered perovskite for the best theoretical prediction of the electron transport layer (ETL) and hole transport layer (HTL) for the perovskite, as well as the best feasible inverted or planar designs for the devices.

1.10 Characterization: principle and analysis

Following are some characterization techniques that are discussed briefly.

13

1.10.1 X-ray diffraction (XRD) analysis

XRD is used to estimate the structure and phases of a substance. The scattered energy of an X-ray beam targeted at a sample is calculated based on its emitted direction as shown in **Fig 1.8**, after the beam has been divided, the scattering, also known as the diffraction peaks, reveals the crystalline structure of the material. The pattern of X-ray diffraction in crystals follows Bragg's law, shown in **equation (1)**:

$$n\lambda = 2d\operatorname{Sin}\theta \dots\dots\dots\dots\dots\dots\dots \text{(1)}$$

Where λ = wavelength of the X-ray beam used, n = integer for the order of peak, θ = Bragg's angle, d = interplanar distance. A plot of peak intensity versus Bragg's angle gives X-ray spectra.
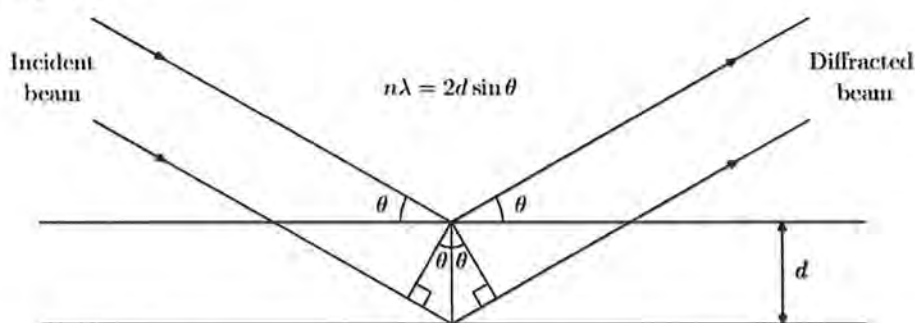
Figure 1.8: Demonstration of Bragg's law[66]

Typically, X-ray diffraction (XRD) studies are performed to get the information about interplanar spacing, lattice parameters and crystallite size.

1.10.2 Scanning electron microscopy (SEM)

SEM is a powerful tool that produces high resolution images of the electronic surface of a variety of materials using an electron beam. It may be used to investigate minute characteristics on the surface of diverse materials (down to 1 µm). The SEM images give information about sample structure and topography. To study the surface morphology, these images could be further magnified by setting the range[67].

1.10.3 Energy dispersive X-ray (EDX) analysis

The elemental composition of the sample is measured by using energy-dispersive X-ray analysis. The same instrument is used for EDX spectra as used for SEM analysis. The electron beam falls on the sample and its energy is transferred, resulting in the excitation of atoms of different materials in EDX analysis. During de-excitation, the atoms are recognized by analyzing the wavelength of emitted X-rays. The particular atoms of the sample are related to each wavelength. A histogram is

formed by collecting all the emitted X-rays in a specific range possible only by the use of a sensitive detector. The histogram gives compositional elements of the sample by decoding in computer software. The concentration of an element in a sample is proportional to the peak intensity of the spectrum[67].

1.10.4 Diffuse reflectance spectroscopy (DRS)

Diffuse reflectance spectroscopy (DRS) is a non-destructive technique used to analyze materials by shining light on the surface of sample and measuring the scattered or reflected light. It provides insights into composition and properties, especially for powdered or complex samples. For DRS, the linear function between concentration and reflectance is plotted by the Kubelka-Munk function as shown in **equation (2)**[68] to calculate band gap of material.

$$F(R) = \frac{(1-R)^2}{2R} \dots\dots\dots\dots\dots\dots\dots\dots\dots \textbf{(2)}$$

Where R is the reflectance after penetration and scattering throughout a non-absorbing material of an infinite depth.

1.11 Device characterization parameters and terminologies of solar cells

The most important parameters used to check the photovoltaic performance of the solar cells are short circuit current (I_{sc}), open-circuit voltage (V_{oc}), and fill factor (FF). These parameters are used to measure I-V characteristics under light illumination. **Fig 1.9** shows the characteristic I-V curve of a solar cell.

1.11.1 I-V characteristics

The necessary electrical measurements of solar cells are the I-V measurements *i.e.*, a plot between measurements of current and the applied voltage. The short-circuit current I_{sc} is measured when the voltage becomes zero, while the open-circuit voltage V_{oc} is measured when the value of current becomes zero.
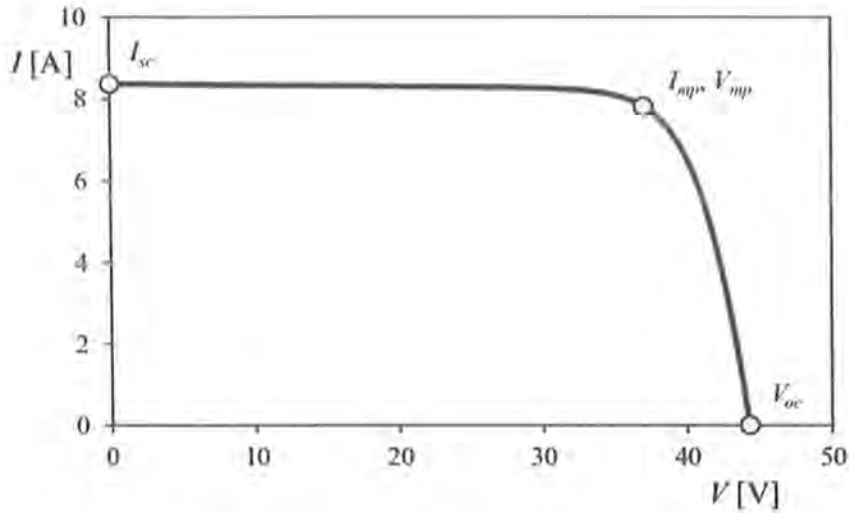
Figure 1.9: *General representation of an I-V curve*[69]

1.11.2 Open circuit voltage (V_{oc})

When the current flowing through the external circuit is zero and resistance is maximal, open circuit voltage is termed as the maximum potential difference that is developed across two electrodes. It is represented as $V = V_{oc}$.

1.11.3 Short-circuit current density (J_{sc})

When solar cell terminals are short-circuited i.e., contacted with each other, the maximum light generated current produced by a solar cell is called short-circuit current density J_{sc}. It gives information regarding charge separation and transport efficiency in the cell, and it is affected by several factors such as the amount of incident photons, optical qualities, reflection, solar spectrum, absorption and solar cell surface area. It is shown in **equation (3)** as:

$$J_{sc} = \frac{I_{sc}}{A} \quad\quad \text{................................... (3)}$$

Where "A" is the effective area of solar cell, "I_{sc}" is the short circuit current. Under 100 mW/cm^2 light illumination, short circuit current ranges from 0.20 to 80 mA/cm^2 for a standard silicon solar cell.

1.11.4 Fill factor (FF)

It is demonstrated as the maximum power point divided by the product of short circuit current and open circuit voltage as shown in **equation (4)**. It provides information about the overall functioning of the cell. Its value is usually between zero and one[70], but it can be represented as % FF.

$$FF = \frac{M_{pp}}{J_{sc}.V_{oc}} \quad \dots\dots\dots\dots\dots\dots\dots\dots\dots \quad (4)$$

1.11.5 Power conversion efficiency (PCE)

The ratio of the highest output power to the photons incident on the device is defined as power conversion efficiency. It compares the amount of power generated by the device to the number of absorbed radiations that shine on the device (η). **Equation (5)** represents the power conversion efficiency of the device.

$$\eta = \frac{J_{sc}.V_{oc}.FF}{P_{in}} \quad \dots\dots\dots\dots\dots\dots\dots\dots \quad (5)$$

1.11.6 Shunt resistance (R_{sh})

Shunt resistance exists between the donor and accepter interface. Shunt resistance causes significant power loss by providing an alternate current channel for the light-generated current. Shunt resistance has the effect of lowering the fill factor. The slope of the I-V curve at the short circuit current point can be used to obtain an approximation of the shunt resistance[71].

1.11.7 Series resistance (R_s)

In a solar cell, series resistance is caused by charge transfer and contact resistance in the semiconductor material. High value of series resistance can reduce the fill factor, circuit current and ultimately power conversion efficiency[72].

1.12 Objectives of Research

The primary objectives of this research are twofold. Firstly, the investigation focuses on the synthesis of $Cs_2SnI_{6-x}Br_x$ films under varying operating temperatures, aiming to observe the intricate relationship between temperature variations and the resulting film characteristics. This analysis will provide crucial insights into the potential use of $Cs_2SnI_{6-x}Br_x$ films as lead-free alternatives in various applications. Secondly, the research involves numerical simulations to assess the viability of eco-friendly Cs_2PtI_6 for solar cell applications. By comparing its simulated performance with conventional solar cell materials, this study contributes to the evaluation of sustainable alternatives in the realm of solar energy.

1.13 Plan of work

To achieve the specified objective, a research plan was established, involving the following approaches. For the preparation of $Cs_2SnI_{6-x}Br_6$ films, the plan involved initially synthesizing the precursor materials, SnI_4 and $CsBr$ films, and then using these precursors for the fabrications of perovskite films at temperatures $100\ ^oC$, $120\ ^oC$ and $140\ ^oC$. For device modelling, SCAPS-1D software would be used. The plan was to use molybdenum trioxide (MoO_3), tin (IV) oxide (SnO_2), and Cs_2PtI_6 as HTL, ETL and absorber layer, FTO and carbon as front and back contact. To enhance device parameters, HTL, ETL and absorber layer thicknesses, along with interface and defect layer parameters, back contact work function, operating temperature, series and shunt resistance would also be optimized.

Chapter 2

Experimental

Pure solvents and reagents are necessary to successfully synthesize perovskite materials. This chapter explains the methods for drying solvent, instrumentation required for characterizations and the procedure for synthesizing precursor materials and respective perovskite films.

2.1 Chemicals and reagents

All the chemicals were used as such without any further purification. Cesium bromide (CsBr, 99.9 %), tin metal (Sn, 99.5 %), iodine crystals (I$_2$, 99.9 %) and glass substrate were purchased from Sigma Aldrich, Germany. Dichloromethane was purchased from Merk, Germany.

2.2 Drying of solvent (dichloromethane)

Dichloromethane was dried by stirring with a small amount of calcium hydride (CaH$_2$) overnight under an inert atmosphere. It was then distilled at its boiling point (39.6 °C) to get dried dichloromethane.

2.3 Synthetic procedure

2.3.1 Synthesis of tin (IV) tetraiodide

To synthesize SnI$_4$, 5 g of Sn powder and 13 g of I$_2$ were taken in a round bottom flask and 50 ml dichloromethane was used as a solvent. It was refluxed for 4-5 hours. To remove excess Sn powder, the hot solution was filtered into another beaker and chilled in an ice bath. Vivid orange crystals of SnI$_4$ were collected via filtration, which were then washed with 5 ml of cold dichloromethane. The crystals were dried overnight in a vacuum oven[73]. Fig 2.1 shows the schematic representation for the synthesis of SnI$_4$.

2.3.2 Synthesis of CsBr films

To synthesize CsBr films, first the glass substrates were washed ultrasonically using acetone, iso-propanol, deionized water and then dried. To deposit CsBr layer on glass substrate, 99.99 percent pure anhydrous CsBr granules were placed in a Tungsten (W) boat of the thermal evaporator, set inside the glove box with a base pressure of 2.6

bar. **Fig 2.2** shows the synthesis of CsBr film. The deposition rate was 5 A/s and the pressure of evaporation was 8.0 x 10^{-7} mbar. CsBr films of 350 nm thickness were formed.
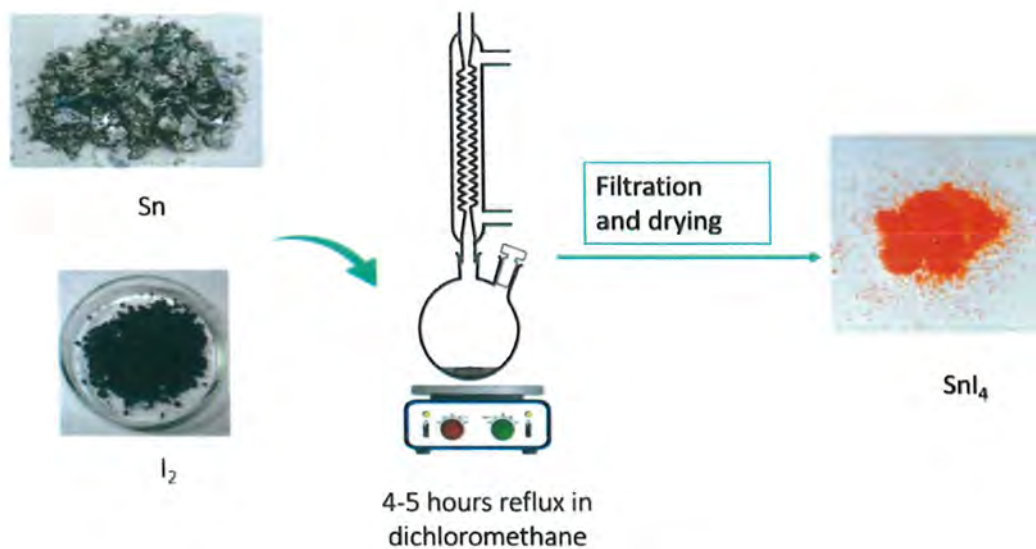
Figure 2.1: *Synthesis of SnI₄*
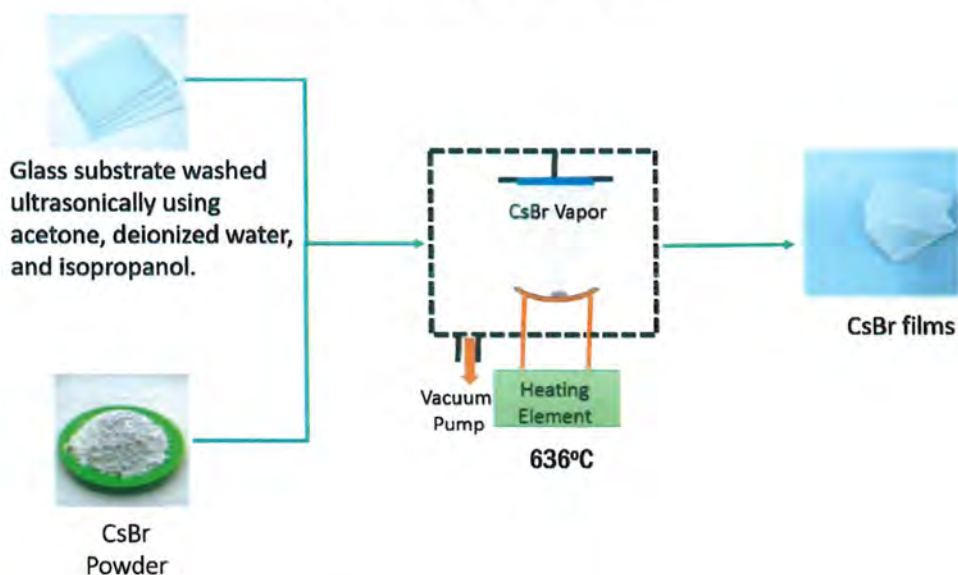
Figure 2.2: *Synthesis of CsBr*

2.3.3 Synthesis of Cs₂SnI₆₋ₓBrₓ films

To synthesize $Cs_2SnI_{6-x}Br_x$ films at different temperatures, SnI_4 along with CsBr film was put in an autoclave and with a heating rate of 5 °C/min, it was heated for two hours at 100 °C, 120 °C, and 140 °C. Black perovskite films at different temperatures

were subsequently formed. **Fig 2.3** shows the schematic representation for the synthesis of perovskite films, and **Fig 2.4** shows the synthesized $Cs_2SnI_{6-x}Br_x$ films.
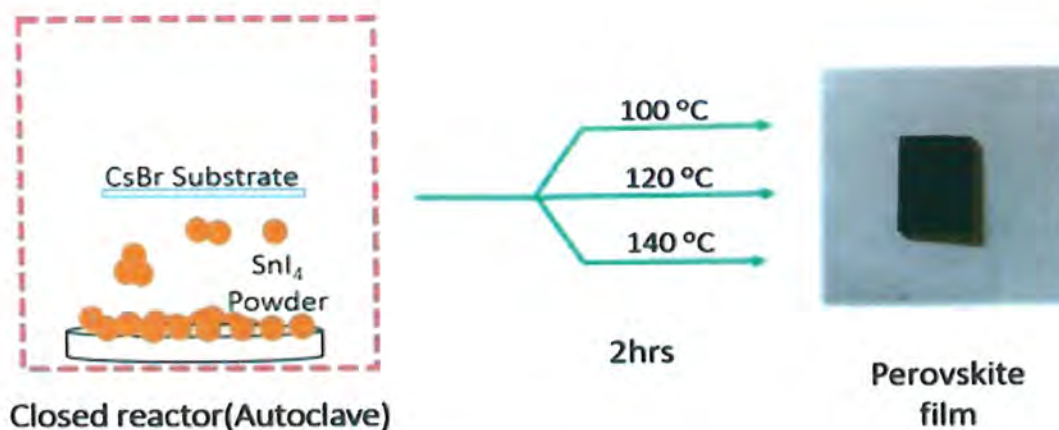
Figure 2.3: Synthesis of $Cs_2SnI_{6-x}Br_x$ films at different temperatures
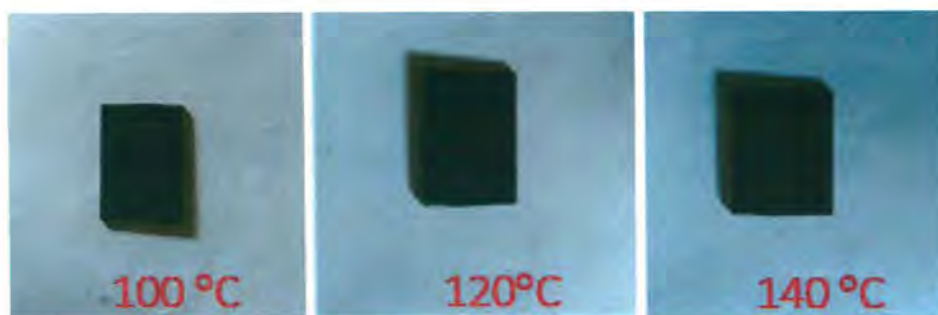
Figure 2.4: Synthesized $Cs_2SnI_{6-x}Br_x$ films at different temperatures

2.4 Characterization techniques

2.4.1 X-ray diffraction analysis

Crystallographic properties of the perovskite films were examined using X-ray diffraction (XRD) with a PAN analytical X'Pert at room temperature employing Cu Kα (1.548 nm) radiation over time. The samples were analysed in the range of 2θ values of 10° to 60°.

2.4.2 Diffused reflectance spectroscopic studies

For diffused reflectance spectroscopic measurements, UV–vis-NIR spectrophotometer (Perkin Elmer lamda 950) was employed (VARIAN, Photometric accuracy is <0.00025 Abs).

2.4.3 Scanning electron microscopy (SEM) and energy dispersive X-ray (EDX) analysis

Scanning electron microscope (SEM) images were recorded by FEI NOVA Nano SEM 450 and EDX elemental mapping with Bruker EDX system at a voltage of 3kV.

2.4.4 Hall measurements

The carrier concentration and mobility in the synthesized materials were measured using Hall effect system (model number: HO-ED-EM-06). The applied current varied between 0.7 to 0.1 A. The strength of magnetic field is adjusted at 2000 gauss by applying potential using source meter (Keithley 2400 source meter SMU instruments).

2.5 Device simulation of Cs_2PtI_6 perovskite solar cell

To model Cs_2PtI_6 solar cell, SCAPS-1D software (version.3.3.10) was utilized. **Fig 2.5** shows the layout of SCAPS-1D panel. Interface layer defect parameters are given in **Table 2.1**. The input parameters for FTO, SnO_2, Cs_2PtI_6, and MoO_3 derived from the literature are shown in **Table 2.2**. The work functions of front contact (FTO) and back contact (carbon) were 4.4 eV and 5.0 eV, respectively. Thermal velocity of both holes and electrons was 1×10^7 cm/s (at 300 K). All simulations were performed under AM 1.5 spectra, constant illumination of 1000 W/m^2, working temperature of 300 K, and shunt and series resistance of 4200 Ω cm^2 and 1 Ω cm^2.

Table 2.1: Interface layers defect parameters

Parameters	HTL/Perovskite interface	Perovskite/ETL interface
Capture cross section electrons (cm^2)	1.00E-19	1.00E-18
Capture cross section holes (cm^2)	1.00E-18	1.00E-19
Reference for defect energy level E_t	Above the highest EV	Above the highest EV
Energy with respect to Reference (eV)	0.600	0.600
Total density (cm^{-2})	1.00E+13	1.00E+13

Table 2.2: *Input parameters of materials used in the device architecture* $FTO/SnO_2/Cs_2PtI_6/MoO_3/C$

Input parameters	FTO	n-SnO$_2$	Cs$_2$PtI$_6$	n-MoO$_3$
Thickness, d (nm)	500	10	300	30
Band gap, E$_g$ (eV)	3.5	3.5	1.37	3
Electron Affinity, χ	4	4	4.3	2.5
Permittivity, ε_r	9	9	4.8	12.5
Electron mobility, μ_n (cm^2/V s)	20	20	62.6	25
Hole mobility, μ_p (cm^2/V s)	10	10	62.6	100
Effective density of states at CB, N$_c$ (cm^{-3})	2.2E+18	2.2E+17	3.0E+14	2.2E+18
Effective density of states at VB, N$_v$ (cm^{-3})	1.8E+19	2.2E+16	1.0E+17	1.8E+19
Density of n-type doping, N$_D$ (cm^{-3})	1E+19	1E+18	1E+12	0
Density of p-type doping, N$_A$ (cm^{-3})	0	0	1E+15	1E-18
Defect density, N$_t$ (cm^{-3})	-	1E+15	1E+17	1E+15
Reference	74	75	50,53	76
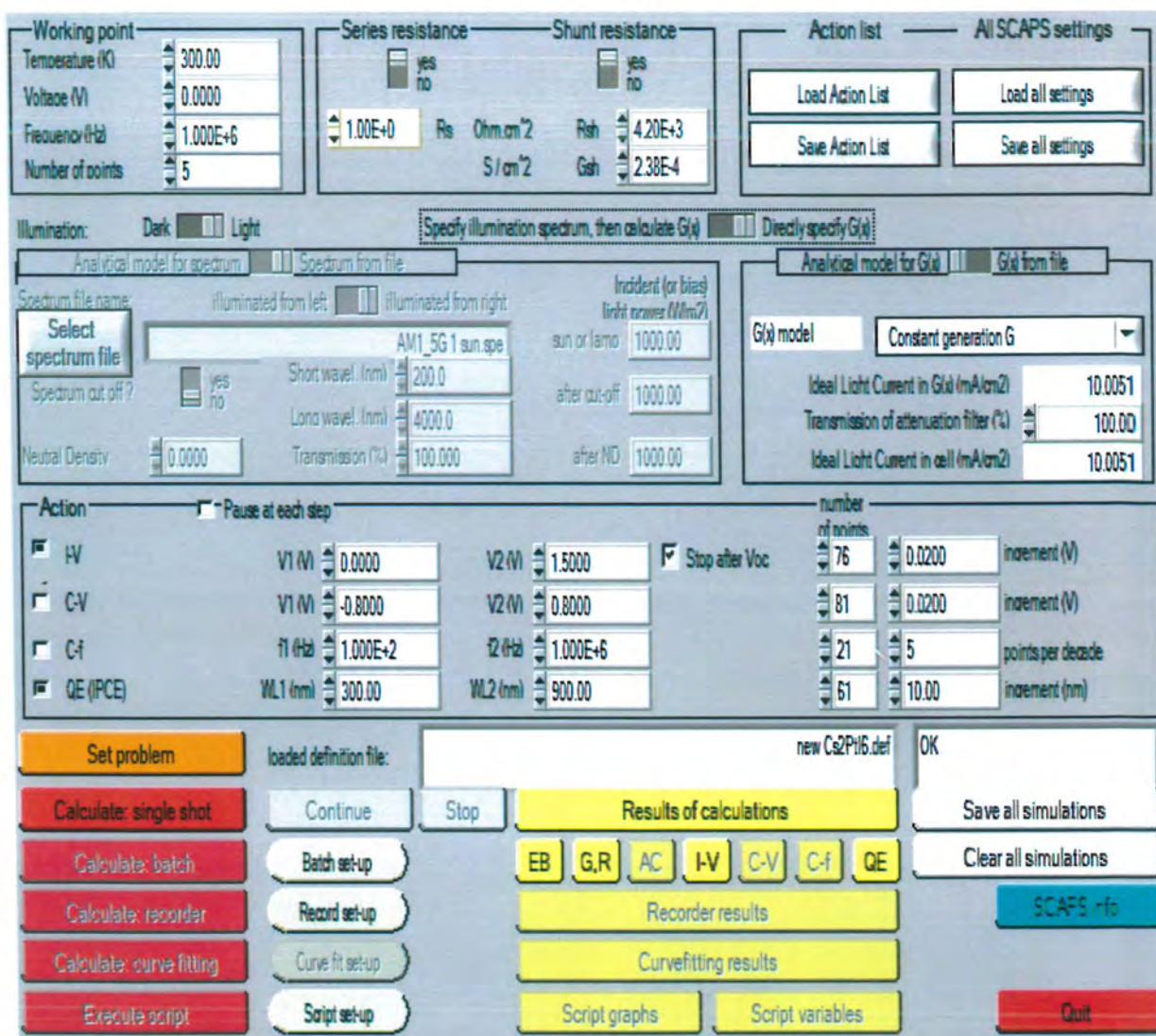
Figure 2.5: *Layout of the SCAPS- 1D*

Chapter 3

Results and Discussion

3.1 Characterization techniques

Structure and phase studies of the materials were carried out by X-ray diffraction (XRD) analysis. Optical analysis was performed using DRS analysis. Morphological studies were done using SEM analysis, while elemental mapping was evaluated using EDX analysis. Hall measurements were employed to assess the electrical characteristics of the films.

3.1.1 X-ray diffraction analysis

X-ray diffraction analysis was used to evaluate crystalline nature and structural identity of all materials. **Fig 3.1** shows the X-ray diffractograms of SnI_4 and CsBr film. The observed peaks in the X-ray diffractograms of synthesized SnI_4 and CsBr aligned precisely with the characteristic 2θ values in the corresponding JCPDS card (PDF# 00-006-0232 and 00-005-0588). This agreement showed that SnI_4 and CsBr film have been successfully formed.
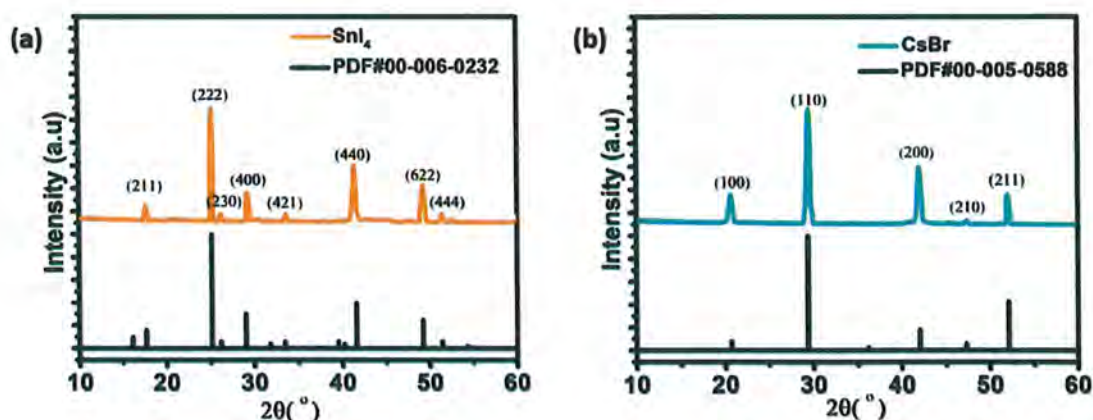
Figure 3.1: *X-ray diffractograms of the synthesized a) SnI_4 and b) CsBr film*

X-ray diffractograms of $Cs_2SnI_{6-x}Br_x$ films at temperatures 100 °C, 120 °C, 140 °C, SnI_4 and CsBr film are shown in **Fig 3.2**. In the XRD pattern of all the perovskite films, precursor peaks at 2θ values corresponding to SnI_4 (25.13, 29.06, 41.58, 49.21) and CsBr (29.36, 42.03, 52.10) were absent. In their place, distinct new peaks at 2θ (26.5, 31.3, 44.77, 53.33, 55.22) were emerged, indicative of the cubic phase, characteristic of perovskite formation[46]. This pattern strongly supports the conclusion

that perovskite formation has indeed taken place. Crystallite size was calculated using the Debye-Scherrer equation, which is given by **equation (6)** as follows:

$$D = K\lambda/\beta cos\theta \dots\dots\dots\dots\dots\dots\dots\dots\dots\dots\dots \textbf{(6)}$$

Where D = crystallite size, K = shape factor (0-0.9), β is full width at half maximum value.
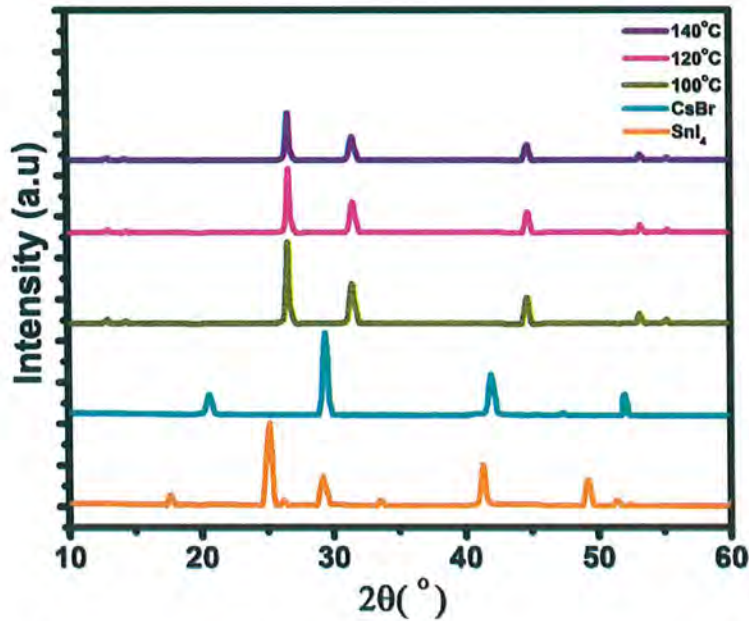
Figure 3.2: *XRD patterns of SnI₄, CsBr and Cs₂SnI₆₋ₓBrₓ films at temperatures 100 °C, 120 °C and 140 °C*

Table 3.1: *Crystallite size of Cs₂SnI₆₋ₓBrₓ films at different temperatures*

Temperature (^{o}C)	Crystallite size (nm)
100	33.4
120	29.2
140	23.6

Table 3.1 shows the calculated crystallite size of synthesized perovskite film. It was observed that as the temperature increased, intensity of peaks decreased, the peaks became broader, which led to a decrease in crystallite size. This trend suggests a temperature-dependent modulation of crystallite growth during the fabrication process.

3.1.2 Diffused reflectance spectroscopy

Diffused reflectance spectroscopy (DRS) analysis was used to gain insights into the structural properties of the films, as changes in reflectance are indicative of shifts in material composition, morphology, or crystal arrangement. **Fig 3.3a** shows the DRS spectra of the synthesized films. The analysis revealed a sharp increase in percent reflectance, a characteristic which suggests that the films possess a high level of crystallinity[46].
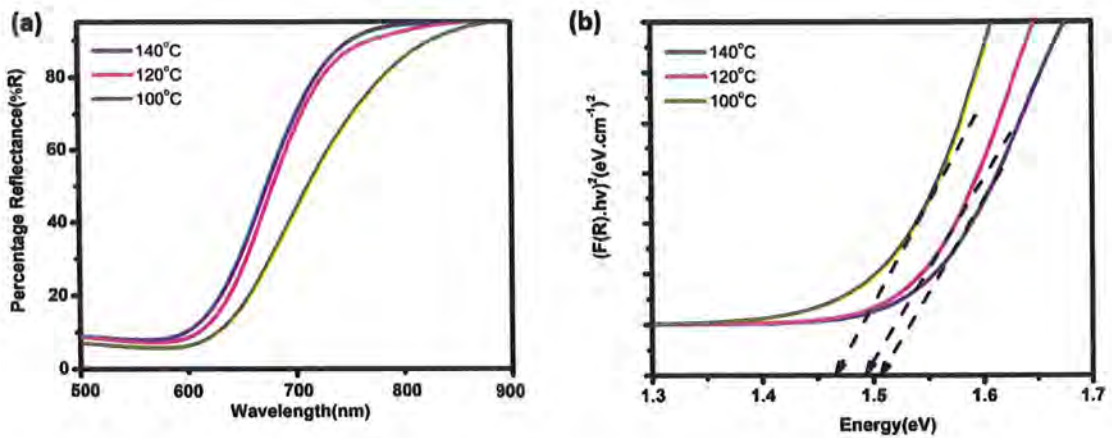
Figure 3.3: a) UV-Vis diffuse reflectance spectra of the synthesized films b) Band gap estimation of films using Kubelka-Munk plot

The band gap of films was calculated with Kubelka-Munk plot, (shown in **Fig 3.3b**) which is a plot between $(F(R).hv)^2$ and hv (photons energy). **Equation (7)** shows the Kubelka Munk equation for direct band gap.

$$(F(R)hv)^2 = A(hv - E_g) \dots\dots\dots\dots\dots\dots\dots\dots (7)$$

Where $F(R)$ is kubelka-munk coefficient, h is Plank's constant, v is frequency, A is proportionality constant and E_g is bandgap energy.

By examining the band gap values at varying deposition temperatures—100 °C, 120 °C, and 140 °C—a distinct trend emerged. **Table 3.2** shows the calculated band gap energy of films. It was seen that as the temperature increased, the calculated band gap also exhibited an incremental increase, with values of 1.47 eV, 1.49 eV, and 1.51 eV, respectively.

This observed relationship between temperature and band gap offers valuable insights into the structural evolution of the films. Specifically, the correlation suggests that the temperature-induced reduction in particle size contributes to the observed increase in band gap. This connection between temperature, particle size, and band gap

behaviour underscores the intriguing sensitivity of films to fabrication conditions, highlighting the intricate interplay between processing parameters and resulting material properties.

Table 3.2: Band gap estimation of films at different temperatures

Temperature ($^{\circ}$C)	Band Gap (eV)
100	1.47
120	1.49
140	1.51

3.1.3 Hall measurements

Hall measurements were employed to assess electrical characteristics of $Cs_2SnI_{6-x}Br_x$ films under different reaction conditions. From these measurements, it was revealed that $Cs_2SnI_{6-x}Br_x$ perovskite is a p-type material. Carrier mobility ranged from 208 to 328 $cm^2V^{-1}s^{-1}$ and carrier concentration from 10^{13} to 10^{16} cm^{-3}, as shown in **Table 3.3**. Mobility variations resulted from surface shape, defect density, and impurities. At the reaction temperature of 140 $^{\circ}$C, the sample with the greatest mobility of 328 $cm^2V^{-1}s^{-1}$ was obtained. These findings show that improving the electrical properties of $Cs_2SnI_{6-x}Br_x$ films requires careful control of the reaction conditions. Hall measurements also improved with the increase in temperature, best film was obtained at 140 $^{\circ}$C.

Table 3.3: Hall measurements of the prepared films

Sample Temperature ($^{\circ}$C)	Type	Hole concentrations (cm^{-3})	Hole mobility ($cm^{-2}V^{-1}s^{-1}$)
100	p	1.14×10^{13}	208
120	p	1.63×10^{14}	231
140	p	7.18×10^{16}	328

3.1.4 Scanning electron microscopy (SEM) and energy dispersive X-Ray (EDX) analysis

Scanning Electron Microscopy (SEM) analysis was conducted on both the CsBr film and the optimized perovskite film (at 140 $^{\circ}$C). The SEM images of films are shown in **Fig 3.4**. The images distinctly revealed contrasting morphologies between the two films, indicating the conversion of CsBr to $Cs_2SnI_{6-x}Br_x$. Notably, the perovskite film

28

exhibited an irregular morphology, indicative of the formation of the perovskite structure. In contrast, the CsBr film appeared remarkably smooth.

The observed differences in morphology provided strong evidence of successful perovskite formation in the optimized film. However, the irregular morphology (randomly dispersed particles) of the perovskite film showed the need for precise parameter control during fabrication. The optimization process should focus on refining these parameters to achieve a more uniform and controlled morphology, which is crucial for enhancing the performance and reliability of the perovskite-based device.
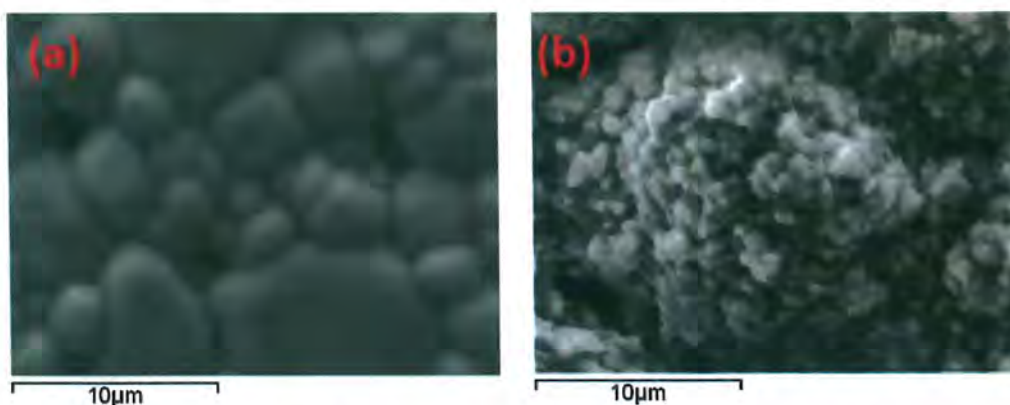
Figure 3.4: SEM images of a) CsBr and b) Perovskite Film

The elemental maps of the films are illustrated in **Fig 3.5**. The EDX mapping of the film showed the presence and distribution of Sn, I, Cs, and Br throughout the film structure.
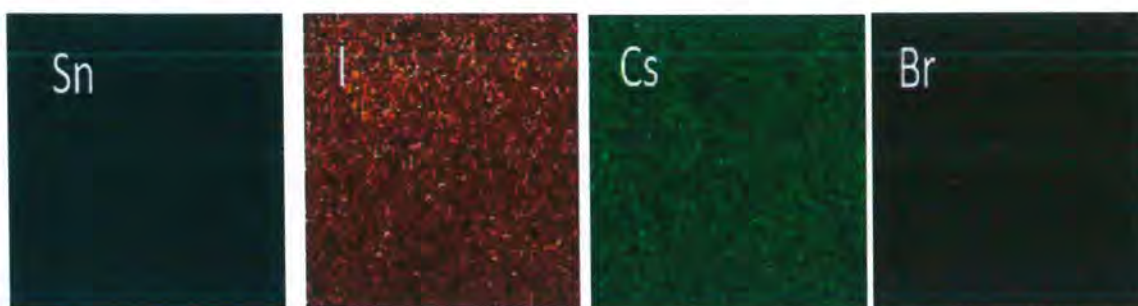
Figure 3.5: Elemental maps of a) Sn b) I c) Cs d) Br

3.2 Numerical simulation of lead-free vacancy ordered Cs$_2$PtI$_6$ based perovskite solar cell using SCAPS-1D[77]

For numerical simulations, SCAPS-1D software version 3.3.10. was used. In this simulation, fluorine doped tin oxide (FTO), tin (IV) oxide (SnO$_2$), cesium platinum (IV) iodide (Cs$_2$PtI$_6$), molybdenum trioxide (MoO$_3$) and carbon (C) were employed as front contact, electron transport layer (ETL), perovskite absorber layer, hole transport

layer (HTL), and back contact. All the input parameters used in this work are shown in **Table 2.1** and **Table 2.2** respectively. All simulations were performed under AM 1.5 spectra, constant illumination 1000 W/m^2, working temperature 300 K, shunt resistance 4200 Ω cm^2 and series resistance 1 Ω cm^2.

3.2.1 Band gap alignment

In order to achieve a higher level of efficiency, the HTL and ETL must have band gap edges that correspond with the valence band maxima (VBM) and conduction band minima (CBM) of the active layers. **Fig 3.6** illustrates the band gap alignment of MoO$_3$, SnO$_2$, and Cs$_2$PtI$_6$, as well as the back and front device contacts. The lowest unoccupied molecular orbital (LUMO) of SnO$_2$ (ETL) is in excellent alignment with the conduction band of Cs$_2$PtI$_6$. Likewise, the highest occupied molecular orbital (HOMO) of MoO$_3$ (HTL) is well-aligned with the valence band level of the absorbing material[77].
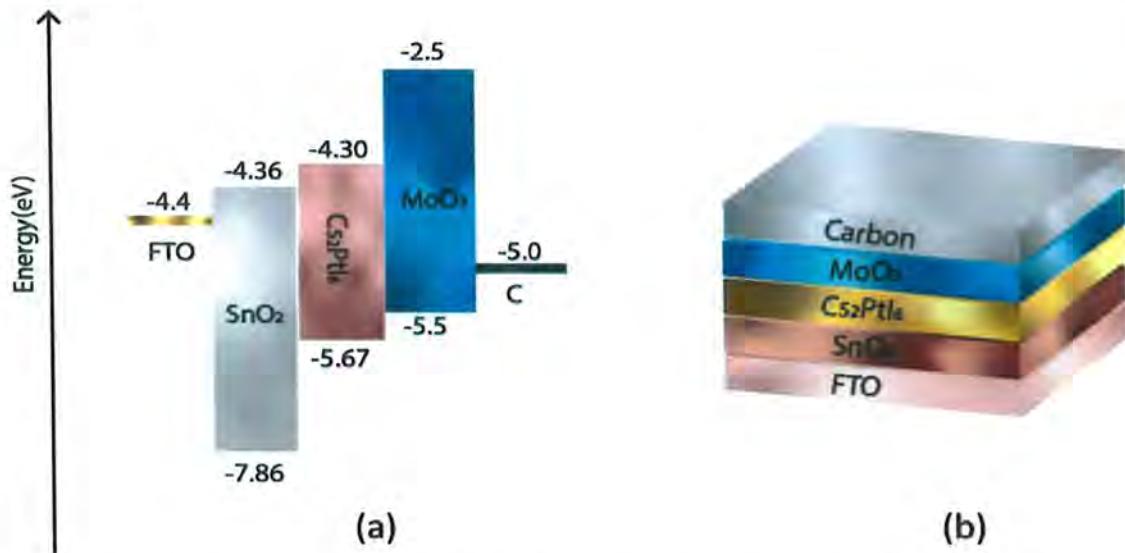
Figure 3.6: *(a) Energy level diagram of FTO, ETL (SnO$_2$), perovskite (Cs$_2$PtI$_6$), HTL (MoO$_3$), back contact C (b) a schematic of device structure of FTO/SnO$_2$/Cs$_2$PtI$_6$/ MoO$_3$/C under AM 1.5 spectra, constant illumination 1000 W/m^2, working temperature 300 K, shunt resistance 4200 Ω cm^2 and series resistance 1 Ω cm^2*

3.2.2 Effect of hole transport layer (HTL) thickness

To ensure that the same number of charge carriers reach terminals instantaneously with a low recombination probability, the HTL is generally kept thicker than the ETL. The impact of HTL thickness on device properties is shown in **Fig 3.7** and **Table 3.4**. Here, MoO$_3$ thickness ranged from 20 to 100 nm.
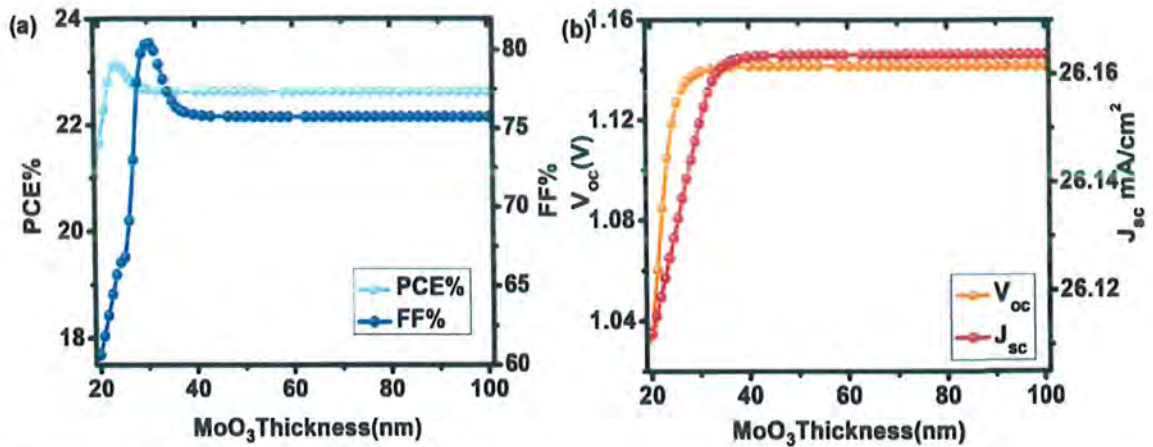
Figure 3.7: *Influence of varying MoO₃ (HTL) thickness (20 – 100 nm) on device performance of configuration FTO/SnO₂/Cs₂PtI₆/MoO₃/C PSC a) Comparison of PCE and FF, b) Comparison of V₍ₒc₎ and J₍ₛc₎*

Table 3.4: *Solar cell parameters at various MoO₃ (electron transport layer) thicknesses (20-100 nm)*

MoO₃ thickness(nm)	V_{oc}(V)	J_{sc}(mA/cm^2)	FF (%)	PCE (%)
20	1.03804	26.14745	79.81242	21.66274
30	1.13943	26.16273	76.03684	22.66695
40	1.14141	26.16343	75.77095	22.62769
50	1.14163	26.16354	75.74602	22.62455
60	1.14164	26.16356	75.74401	22.62431
70	1.14165	26.16357	75.74390	22.62434
80	1.14165	26.16358	75.74386	22.62434
90	1.14165	26.16360	75.74384	22.62435
100	1.14165	26.16363	75.74383	22.62436

Both J_{sc} and V_{oc} increased with an increase in MoO₃ thickness, reaching saturation at 32 nm with a maximum value of 26.163 mA/cm^2 and 1.14 V, respectively. PCE and FF also increased with increasing HTL thickness until reaching their respective peak values, after which these reduced to a constant value.

A thin HTL can cause current leakage and low shunt resistance can occur, resulting in a lower FF[78]. In this case, FF decreased after reaching the highest FF value

of 80.44 % at 22 nm. It could be because by further increasing HTL thickness, series resistance also increased, causing the FF to drop to 75.74 % at 60 nm and becoming constant[78]. At 24 nm, the maximum efficiency of 23.13 %, V_{oc} of 1.118 V, J_{sc} of 26.158 mA/cm^2, and FF of 79.105 % was obtained. Thus, the optimum HTL thickness of 24 nm was utilized for this work.

3.2.3 Effect of absorbing layer thickness

In designing a solar cell, the thickness of the perovskite is crucial because it directly affects the device performance. As electron-hole pair generation occurs in the absorbing layer, increasing perovskite thickness increases incident light absorption and generates more electron-hole pairs. This increases the PCE, but only up to a certain point, after which it degrades. Thus, the perovskite thickness should not exceed the carrier diffusion length; otherwise, recombination density would increase. The influence of absorbing layer thickness on PCE, J_{sc}, V_{oc}, and FF is shown in **Table 3.5** and **Fig 3.8**. Here, the Cs_2PtI_6 thickness was varied from 100 nm to 1000 nm.

Table 3.5: Effect of Cs_2PtI_6 (absorber layer) thickness (100-1000 nm) on device parameters

Cs_2PtI_6 thickness(nm)	V_{oc}(V)	J_{sc}(mA/cm^2)	FF (%)	PCE (%)
100	1.10674	14.81709	84.20089	13.80776
200	1.11805	22.22641	82.05535	20.39087
300	1.11849	26.15861	79.10591	23.14497
400	1.11550	28.34408	75.29937	23.80797
500	1.11107	29.57439	70.60756	23.20115
600	1.10594	30.20621	65.18559	21.77602
700	1.10035	30.36836	59.37677	19.84124
800	1.09450	30.04252	53.49356	17.58954
900	1.08850	29.11874	47.98291	15.20860
1000	1.07210	28.54397	43.29185	13.0112

J_{sc} increased as perovskite thickness increased. Because Cs_2PtI_6 has a higher absorption coefficient (4×10^5cm^{-1})[51], increasing thickness allows more light to be absorbed, resulting in more electron-hole pair generation. As the length of charge

carrier diffusion in these perovskites is longer, these electron-hole pairs can reach the corresponding electrodes to generate power[79]. At 680 nm, J_{sc} reached a maximum of 30.37 mA/cm^2 before decreasing. These findings are consistent with the previously reported data[54].
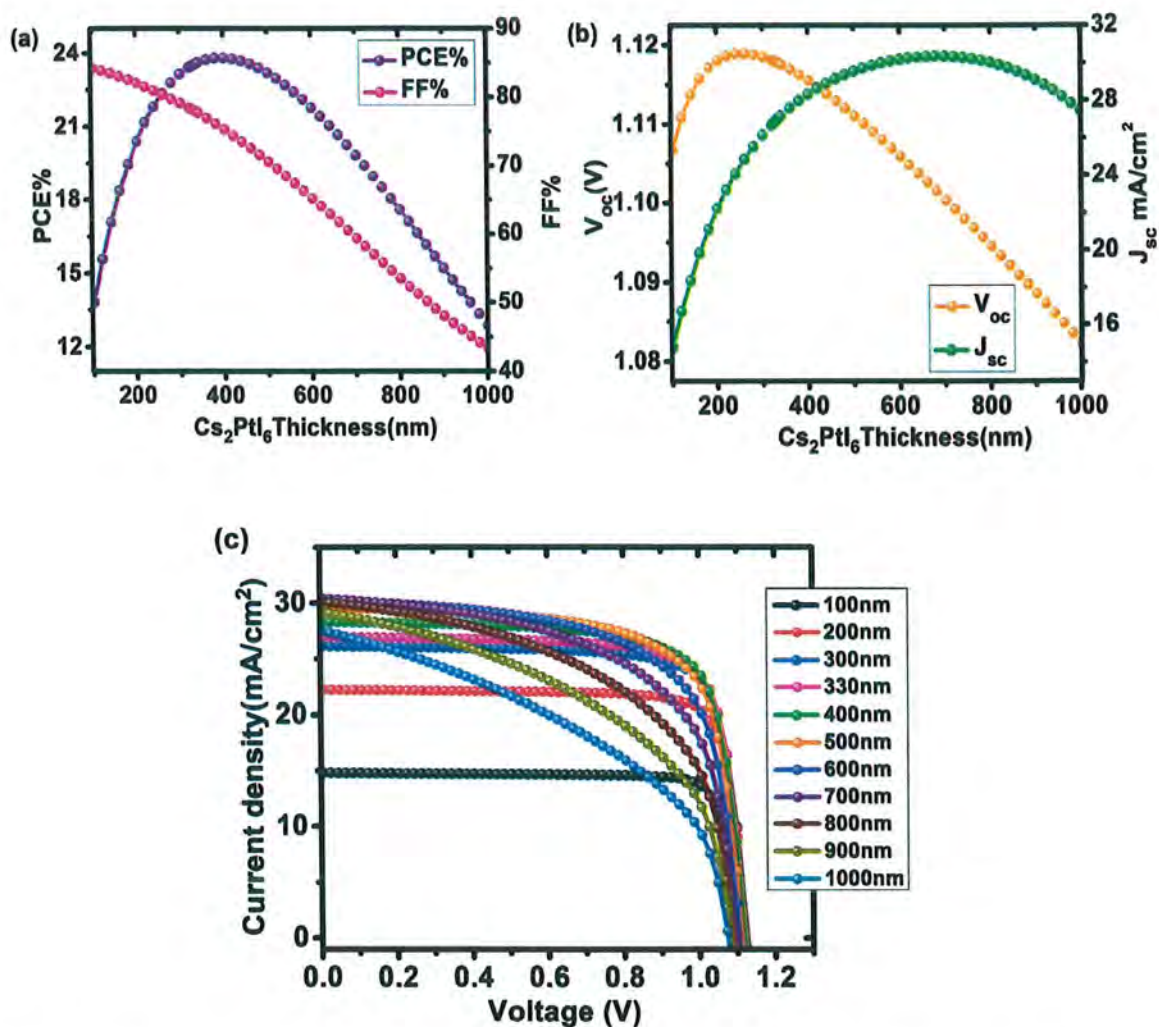
Figure 3.8: *Impact of changing Cs$_2$PtI$_6$ (absorber layer) thickness (100-1000 nm) on device performance a) PCE and FF, b) V$_{oc}$ and J$_{sc}$, c) Comparison of J-V curves at different Cs$_2$PtI$_6$ thicknesses*

PCE also increased as the thickness increased, reaching a maximum value of 23.8 % at 400 nm, after which it decreased. It is because as the thickness increases, due to a higher absorption coefficient, a higher number of charge carriers are generated, which results in an increased efficiency. Following this optimal thickness, despite the higher level of electron and hole pair generation, the perovskite thickness exceeds the carrier diffusion length of electrons and holes, which then results in increased

recombination rates and decreased efficiency. When thickness increases, so do pinholes, cracks, and traps, causing a decrease in PCE[79].

V_{oc} increased with an increase in perovskite thickness until it reached a maximum of 1.11 V at 260 nm, after which it dropped precipitously. It is affected by cracks, pinholes, and other layer defects and is dependent on surface morphology. The absorber layer is relatively thinner during the early rise in V_{oc}, resulting in a lower recombination rate. Furthermore, as the length of the diffusion carrier increases, so does the value of the dark saturation current. This slower recombination rate eventually leads to a higher concentration of carriers, which raises the light-generated current. However, as the thickness of the absorbing layer continues to increase, the recombination rate also increases, causing the V_{oc} to have a sharp decrease[79].

The FF relates to charge route resistance and represents the efficiency with which holes and electrons transit the cell without loss[80-81]. As the perovskite thickness increased, the fill factor decreased. FF decreased from 78.3 % at 100 nm to 43.29 % at 1000 nm as the thickness increased. For this device, an absorber layer thickness of 330 nm was taken.

3.2.4 Effect of electron transport layer (ETL) thickness

The dependence of solar cell properties on ETL (SnO_2) was studied by varying the thickness of the electron transport layer from 10 nm to 100 nm. To prevent incident photons from being absorbed and producing election-hole pairs in the electron transport layer, it is common practice to keep the n-type layer (ETL) thinner than the equivalent p-type layer (HTL). ETL is also kept thinner to allow incident photons to pass through to the absorber and HTLs beneath it. The influence of ETL thickness change on cell metrics is depicted in **Fig 3.9** and **Table 3.6**.

By increasing ETL thickness, no improvement in cell metrics was observed. PCE, V_{oc}, J_{sc}, and FF were 23.52 %, 1.11782 V, 26.95 mA/cm^2, and 78.07601 % at 10 nm, and 23.49 %, 1.11780 V, 26.93 mA/cm^2, and 78.07656 % at 100 nm, respectively. With the increase in ETL thickness, the change in V_{oc} was insignificant (from 1.11782 V to 1.11780 V, a loss of only 0.0017 %), indicating that by varying the thickness of ETL, charge carrier leakage at the interface is limited. When the thickness of a device grows, fewer electron-hole pairs are formed, and charge carrier recombination occurs, resulting in a drop in overall device efficiency. In this work, device has an ETL

thickness of 10 nm, with the PCE of 23.52 %, J_{sc} of 26.95 mA/cm^2, V_{oc} of 1.1178 V, and FF of 78.076 %.
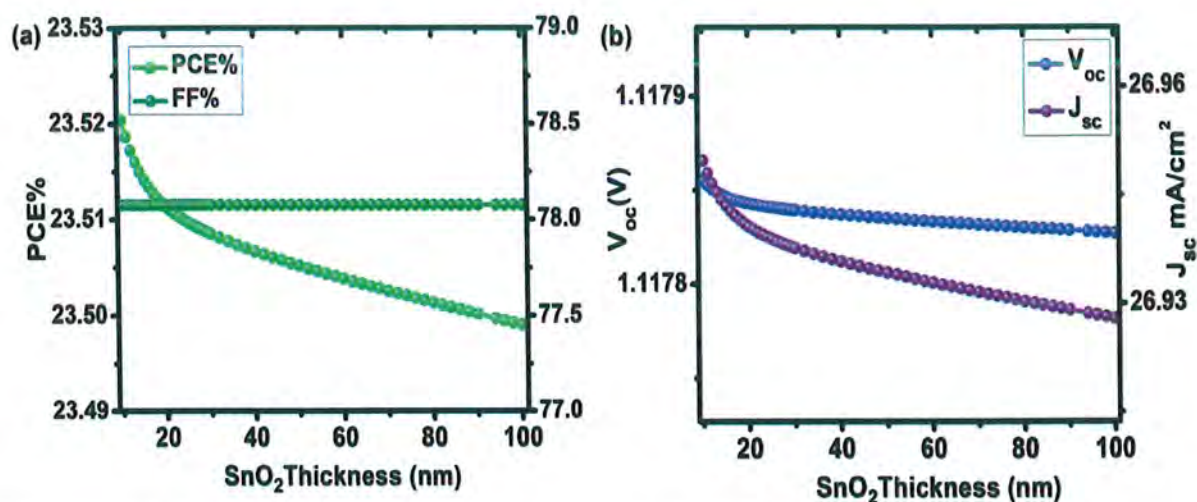
Figure 3.9: *Device performance of configuration FTO/SnO₂/Cs₂PtI₆/MoO₃/C PSC as a function of increasing SnO₂ (ETL) thickness (10-100 nm) a) PCE and FF, b) V_{oc} and J_{sc}*

Table 3.6: *Effect of SnO₂ thickness (10-100 nm) on device parameters*

SnO₂thickness(nm)	V_{oc}(V)	J_{sc}(mA/cm^2)	FF (%)	PCE (%)
10	1.11782	26.94972	78.07601	23.52040
20	1.11781	26.93964	78.07601	23.51135
30	1.11781	26.93640	78.07619	23.50851
40	1.11780	26.93434	78.07628	23.50669
50	1.11780	26.93265	78.07634	23.50519
60	1.11780	26.93113	78.07640	23.50385
70	1.11780	26.92970	78.07644	23.50258
80	1.11780	26.92834	78.07648	23.50137
90	1.11780	26.92701	78.07653	23.50020
100	1.11780	26.92572	78.07656	23.49906

3.2.5 Effect of perovskite (absorber) layer defect density

The optoelectronic properties of an absorbent layer are highly dependent on its preparation method, thickness, and analysis methodologies. Furthermore, defects in the

system could change these properties. Defects were introduced into the absorber layer to make this device appear more realistic. The defect density ranged from 10^{14}-10^{20} cm^{-3}. **Fig 3.10** depicts the effect of Cs_2PtI_6 defect density on cell parameters.
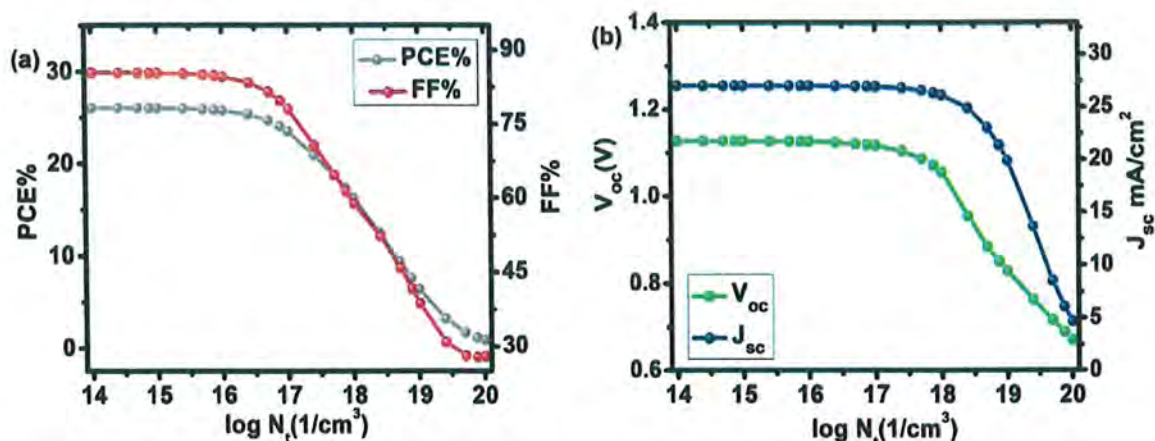
Figure 3.10: *Effect of Cs_2PtI_6 (absorber layer) defect density (10^{14}-10^{20} cm^{-3}) on device parameters a) PCE and FF, b) V_{oc} and J_{sc}*

It was observed that the recombination rate increased and all cell characteristics decreased (as the number of cracks and pinholes increase) with an increase in N_t. An efficiency of 26 % was observed with a defect density of 1×10^{15} cm^{-3}. **Table 3.7** shows the effect of defect density on device parameters. A defect density of 1×10^{17} cm^{-3} was chosen for the device, which yielded an efficiency of 23.5 %.

Table 3.7: *Solar cell parameters at various Cs_2PtI_6 (perovskite absorber layer) defect densities (N_t) for configuration $FTO/SnO_2/Cs_2PtI_6/MoO_3/C$*

Defect Density (cm^{-3})	V_{oc}(V)	J_{sc}(mA/cm^2)	FF (%)	PCE (%)
1×10^{14}	1.1287	27.0396	85.37	26.05
1×10^{15}	1.1286	27.0788	85.29	26.03
1×10^{16}	1.1275	27.0307	84.55	25.77
1×10^{17}	1.1178	26.9497	78.08	23.52
1×10^{18}	1.0560	26.1602	58.83	16.25
1×10^{19}	0.8291	19.9050	38.68	6.38
1×10^{20}	0.6708	4.6933	27.87	0.88

3.2.6 Effect of interface defect density

Due to a mismatch in the crystallographic structures of the ETL, HTL, and absorbing layer, interfaces with a plethora of dislocations could form, hence reducing

junction quality and triggering recombination. The defect density was varied between 10^{12} cm^{-3} and 10^{18} cm^{-3} to explore the global impact of interface defect density on cell performance. **Table 3.8, 3.9** and **Fig 3.11** show the effect of interface (HTL/perovskite and ETL/perovskite) defect density on device performance.

Table 3.8: Effect of MoO$_3$/Cs$_2$PtI$_6$ (HTL/P) interface defect density (cm^{-3}) on device parameters

MoO$_3$/Cs$_2$PtI$_6$ interface defect density (cm^{-3})	V$_{oc}$ (V)	J$_{sc}$ (mA/cm^2)	FF (%)	PCE (%)
1×10^{12}	1.15633	26.94972	76.42912	23.81734
1×10^{13}	1.11782	26.94972	78.07601	23.52040
1×10^{14}	1.06173	26.94966	79.65281	22.79119
1×10^{15}	1.00249	26.94912	80.82039	21.83463
1×10^{16}	0.94543	26.94393	81.10092	20.65927
1×10^{17}	0.90275	26.90611	80.47660	19.54732
1×10^{18}	0.88832	26.83425	79.90022	19.03904

Table 3.9: Effect of SnO$_2$/ Cs$_2$PtI$_6$ (ETL/P) interface defect density (cm^{-3}) on device parameters

SnO$_2$ / Cs$_2$PtI$_6$ interface defect density (cm^{-3})	V$_{oc}$ (V)	J$_{sc}$ (mA/cm^2)	FF (%)	PCE (%)
1×10^{12}	1.11782	26.94972	78.07603	23.52041
1×10^{13}	1.11782	26.94972	78.07601	23.52040
1×10^{14}	1.11782	26.94966	78.07582	23.52029
1×10^{15}	1.11782	26.94908	78.07392	23.51917
1×10^{16}	1.11780	26.94339	78.05526	23.50810
1×10^{17}	1.11760	26.89142	77.88737	23.40806
1×10^{18}	1.11660	26.62564	77.09278	22.91991

There was no significant change in PCE and V$_{oc}$ when the defect density of the ETL/Perovskite layer (SnO$_2$/Cs$_2$PtI$_6$) was varied. However, with the increase in the interface defect density of the HTL/Perovskite layer (MoO$_3$/Cs$_2$PtI$_6$), the efficiency and V$_{oc}$ drastically degraded. The PCE decreased from 23.8 % at N$_t$ 10^{12} cm^{-3} to 19.04 % at 10^{18} N$_t$. V$_{oc}$ decreased by 23 %, from 1.156 V to 0.888 V. As N$_t$ increased, there was

no discernible change in J_{sc}. By increasing the N_t of the HTL/P layer to 10^{18} cm^{-3} (from 26.94 mA/cm^2 to 26.62 mA/cm^2), J_{sc} decreased by 1.19 %. Both interfaces have an effect on the fill factor. The fill factor decreased from 78.08 % to 77.08 % when ETL/perovskite defects increased. In the case of the HTL/Perovskite layer, the defect density increased from 76.42 % to an all-time high of 81.2 % at N_t 10^{15} cm^{-3}, before decreasing to 79.90 % at defect density 10^{18} cm^{-3}. A defect density of 10^{13} cm^{-3} for both device interfaces was selected.
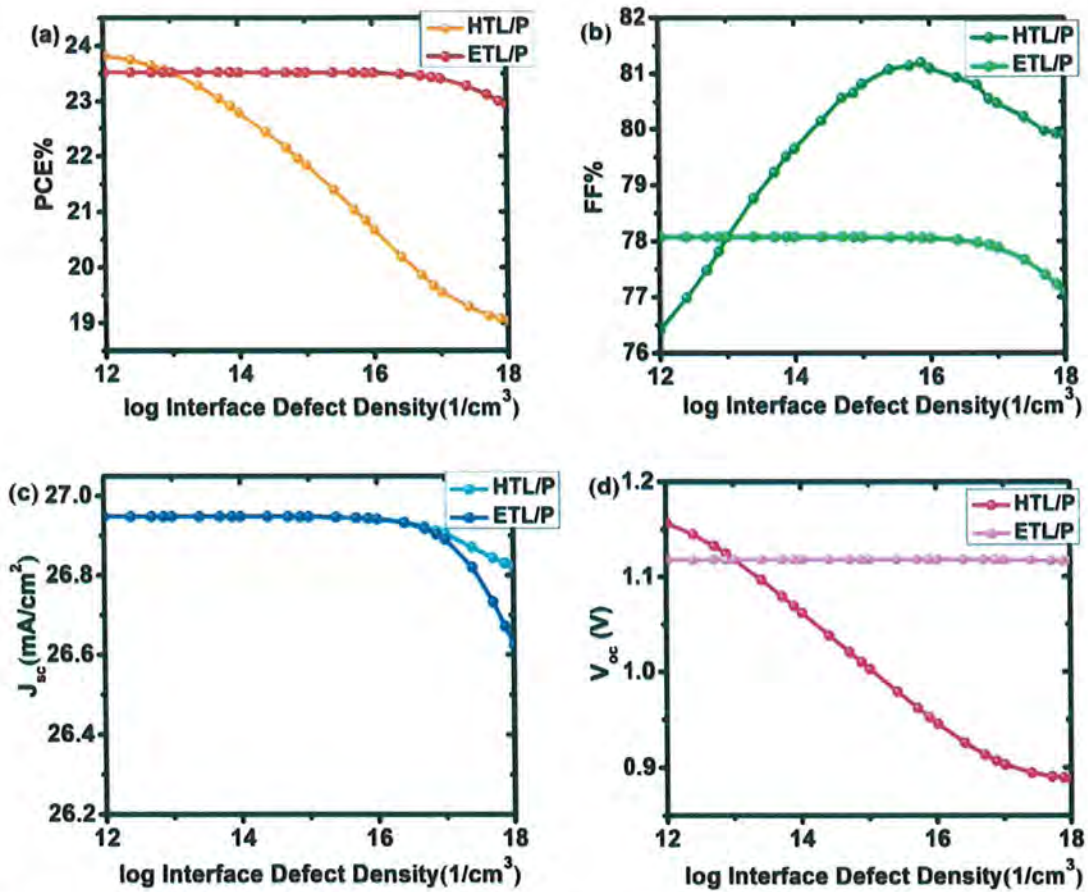
Figure 3.11: *Solar cell output as a function of varying defect density N_t (10^{12}-10^{18} cm^{-3}) of interfaces MoO$_3$/Cs$_2$PtI$_6$ (HTL/P) and SnO$_2$/Cs$_2$PtI$_6$ (ETL/P) a) Efficiency (PCE), b) Fill factor (FF), c) Short circuit current density (J_{sc}) and d) Open circuit voltage (V_{oc})*

3.2.7 Effect of temperature

Temperature has a direct effect on hole mobility, electron mobility, and carrier concentration, all of which affect cell performance[82]. The device performance was investigated at temperatures ranging from 290 K to 400 K. **Equation (8)** shows the effect of temperature on V_{oc}[83].

$$V_{oc} = \frac{nKT}{q} log \left(\frac{J_{sc}}{J_0} + 1 \right) \dots\dots\dots\dots\dots\dots\dots\dots\dots\dots\dots (8)$$

Where V_{oc} is open circuit voltage, K is Boltzmann constant, q is the electronic charge, n is ideality constant, T is temperature, J_0 is reverse saturation current and J_{sc} is current density. It has been observed that with the increase in the operating temperature, reverse saturation current density increases, and V_{oc} decreases exponentially[84]. **Table 3.10** and **Fig 3.12** depicts the effect of temperature on device performance. All cell metrics degraded with an increase in temperature.

Table 3.10: *Effect of working temperature on device parameters*

Temperature (K)	V_{oc} (V)	J_{sc} (mA/cm^2)	FF (%)	PCE (%)
290	1.12295	26.95364	78.31294	23.70195
300	1.11782	26.95159	78.07601	23.52040
310	1.11217	26.94933	77.48610	23.22262
320	1.10579	26.94705	76.73043	22.86239
330	1.09967	26.94465	75.75912	22.42562
340	1.09090	26.94222	74.70142	21.95415
350	1.08231	26.93983	73.66265	21.47668
360	1.07284	26.93748	72.72965	21.01716
370	1.06255	26.93509	71.90821	20.57862
380	1.05121	26.93278	71.1901	20.15398
390	1.03896	26.93056	70.54729	19.73767
400	1.02557	26.92862	69.98351	19.32622

V_{oc} decreased from 1.12295 V at 290 K to 1.02557 V at 400 K. The FF decreased from 78.31 % to 69.98 %. There was no discernible change in the short circuit current density of device. It decreased by 0.09 %, from 26.9536 mA/cm^2 to 26.9282 mA/cm^2. The PCE fell from 23.7 % to 19.0 %. As the temperature rises, the phonons are triggered, increasing charge carrier scattering, this modifies the material conductivity. As a result, overall performance decreased. An optimal working temperature of 300 K was selected for the device, resulting in a PCE of 23.52 %, a V_{oc} of 1.11782 V, a J_{sc} of 26.9519 mA/cm^2 and a FF of 78.07 %.
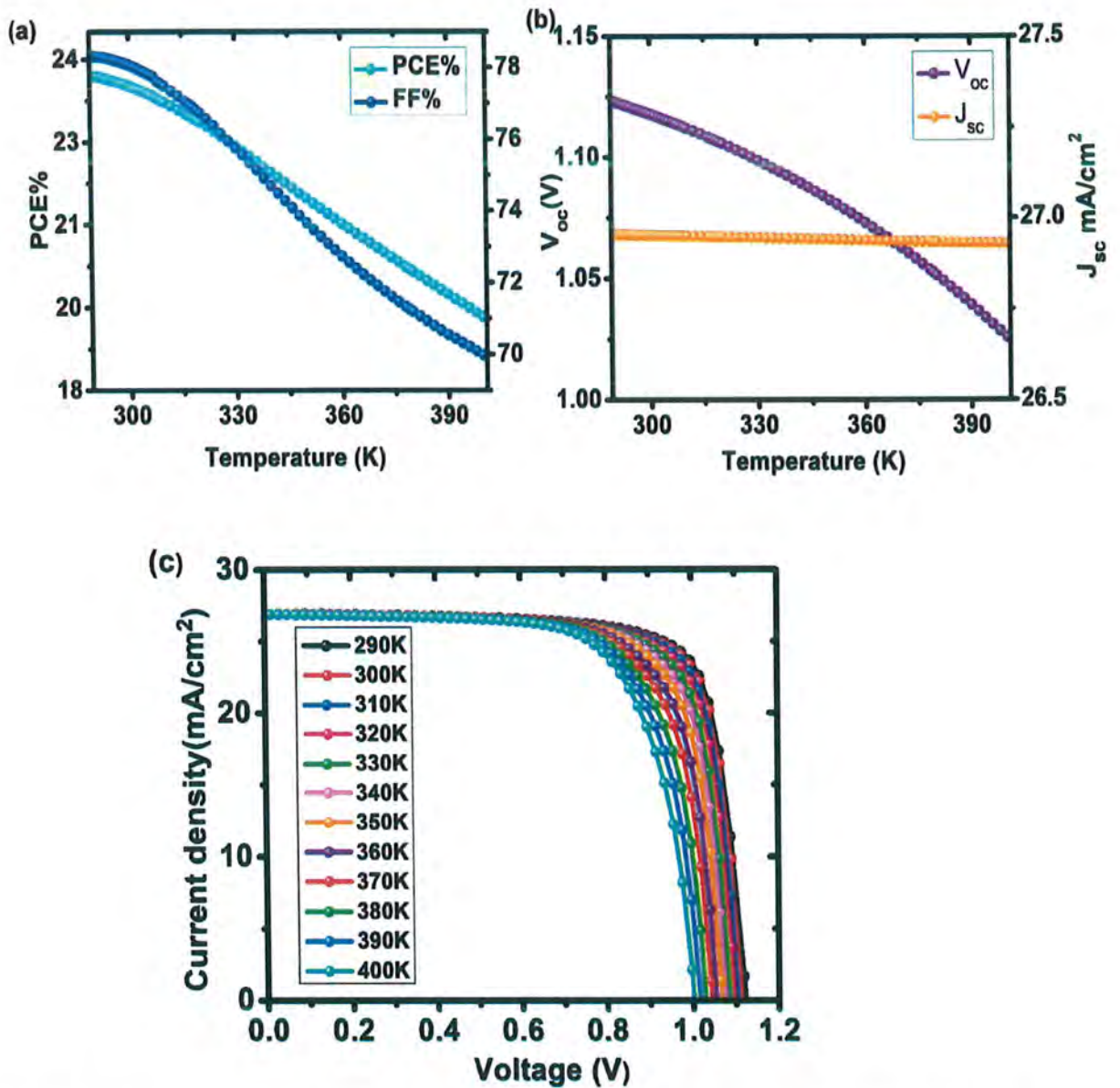
Figure 3.12: *Influence of changing operating temperature (290-400 K) on device performance a) PCE and FF, b) V_{oc} and J_{sc}, c) a comparison of J-V curves of device at different temperatures*

3.2.8 Effect of series and shunt resistance on device parameters

Device performance is immensely influenced by both series and shunt resistance. Series resistance is due to interfaces, back and front contact, and resistance to flow of current while R_{sh} is the aftereffect of reverse saturation current. Both high R_{sh} and low R_s are likely to deliver better device performance. The effect of R_s and R_{sh} on device parameters was studied by altering values between 0.01-50 Ω cm^2 and 10-

10000 Ω cm^2. **Fig 3.13** shows the effect of R$_s$ and R$_{sh}$ on solar cell parameters
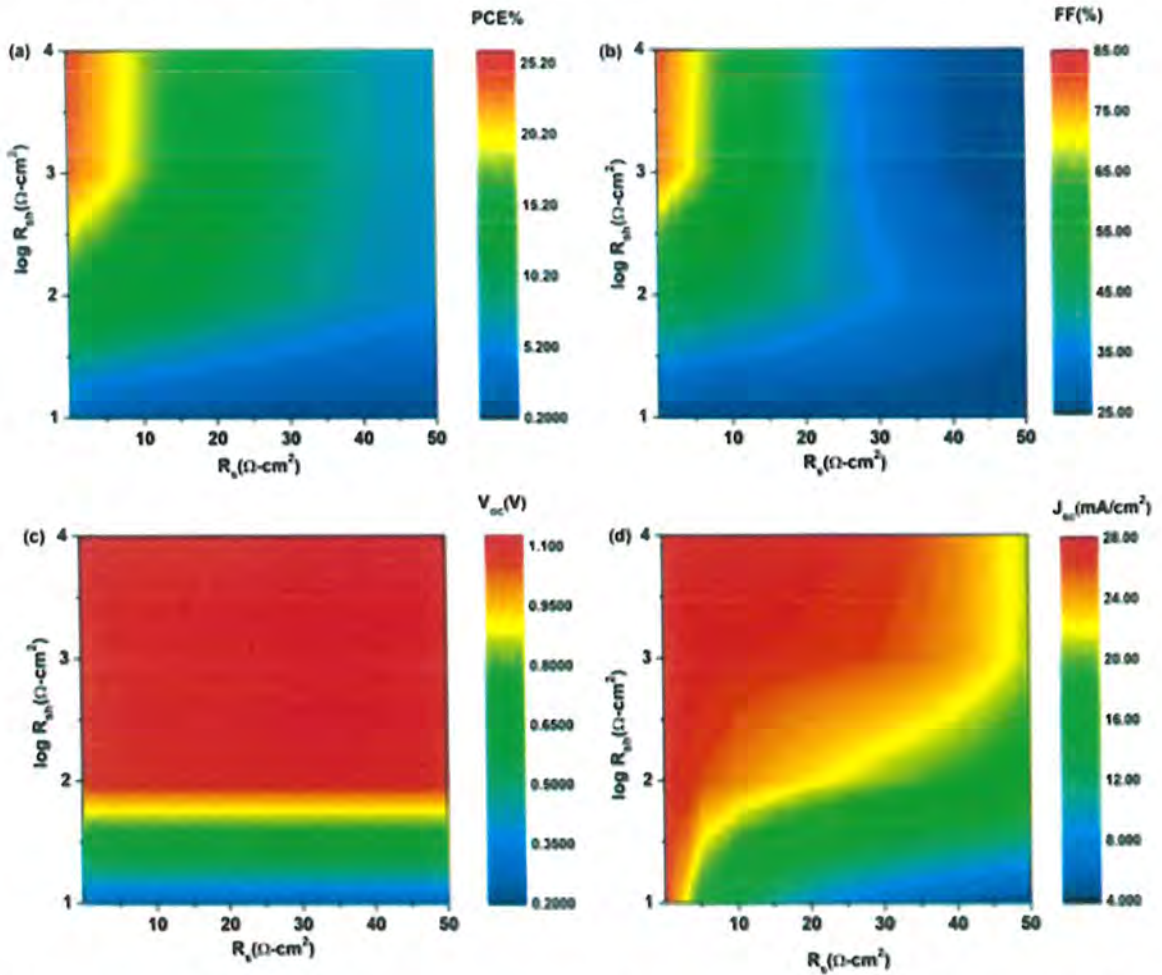
Figure 3.13: *Device parameters as function of series resistance R$_s$ (0.01 to 50 Ω cm^2) and shunt resistance R$_{sh}$ (10 to 10000 Ω cm^2) a) PCE, b) FF, c) V$_{oc}$ and d) J$_{sc}$*

V$_{oc}$ was not affected by R$_s$ but it increased with an increase in R$_{sh}$ but only up to a certain extent, after which it saturated. **Equation (9)** can be used to understand the effect of series resistance on device performance[83].

$$I_{sc} = I_L + I_O\left(e^{\frac{V_{oc}q}{nKT}} - 1\right) - \frac{V_{oc} + I_{sc}R_S}{R_{Sh}} \dots\dots\dots\dots\dots\dots (9)$$

Where I$_{sc}$ is short circuit current, R$_{sh}$ is shunt resistance, R$_s$ is series resistance, I$_L$ is light-induced current, I$_o$ is reverse saturation current, V_{oc} is open circuit voltage, K is Boltzmann constant, q is the electronic charge, n is ideality constant, and T is temperature. According to the above equation, when series resistance increases, short circuit current will decrease. This would have a direct effect on the efficiency and FF. J$_{sc}$ decreasesd at higher R$_s$ values. FF is greatly affected by increasing R$_s$ and decreasing R$_{sh}$ as it decreased from 85 % to 25 %. As a consequence of this rapid decline in FF, PCE decreased from 25 % to 0.3 %.

3.2.9 Quantum efficiency studies

Quantum efficiency (QE) is the probability that an incident photon will transfer an electron to the external circuit of the device. Yet, this property is independent of the incident spectrum. **Fig 3.14** demonstrates the effect of absorbing layer thickness on quantum efficiency for wavelengths between 300 nm and 900 nm.
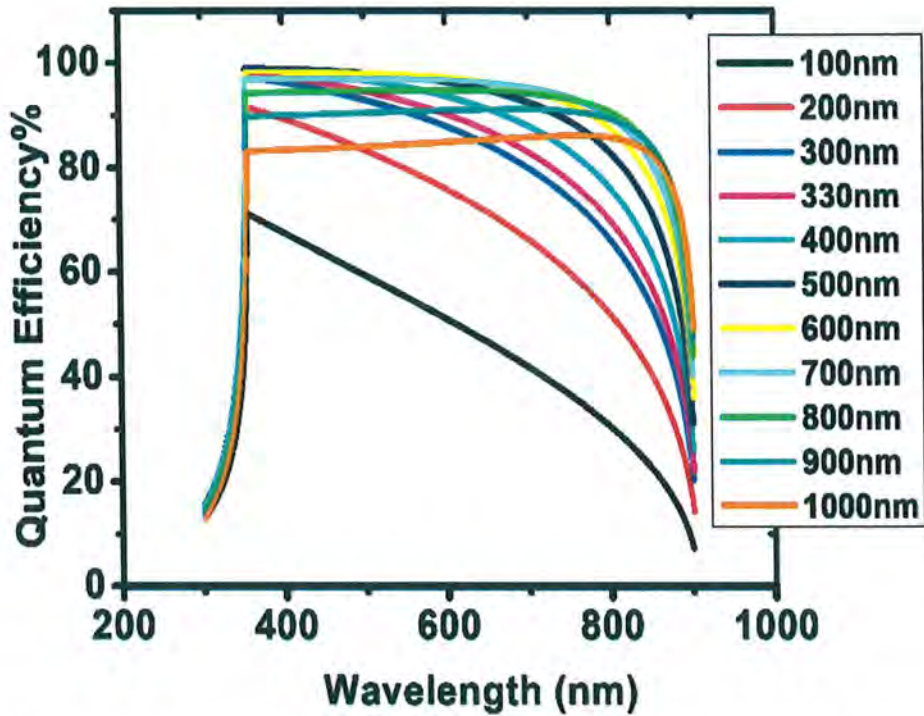
Figure 3.14: *Quantum efficiency of device configuration FTO/SnO₂/Cs₂PtI₆/MoO₃/C at different Cs₂PtI₆ thicknesses (100 – 1000 nm)*

QE increased with increasing perovskite thickness up to a maximum of 98.9 % before decreasing. At 100 nm, the QE was 70 %. At 400 nm, the concentration increased from 91.6 % at 200 nm to 98.85 %. A further increase in thickness did not result in a significant increase in QE, as QE at 500 nm was already 98.9 %. By further increasing the thickness to 1000 nm, QE decreased to 86.1 %. In the range of 354-550 nm, the highest quantum efficiency was observed. Maximum QE was observed at the wavelength 354.5 nm. This high QE of perovskite is due to its high absorption coefficient $(4\times10^5 cm^{-1})$[51]. This study demonstrates that Cs₂PtI₆ is optically active and may have additional applications in photovoltaics.

3.2.10 Effect of back contact on device parameters

The back contact of solar cells is essential to their performance because it absorbs electrons from the absorbing layer. For ohmic contact with the HTL or the absorber layer, a high work function is necessary. **Fig 3.15** illustrates the effect of the back contact work function on the device performance. Cu, Ni, Ag, Fe, graphene oxide, and carbon were used as back contact materials in this device.

As work function increased, efficiency grew, beginning at 13.14 % with Cu as the back contact and reaching a high of 23.52 % with carbon as the back contact. The other cell metrics likewise improved when the back-contact work function increased. As the work function of the back contact increases, the barrier height for charge carriers at the back contact decreases, leading to an overall improvement in cell characteristics. **Table 3.11** compares cell properties to the work function of the back contact.

Table 3.11: Solar cell parameters at different values of back contact work function (eV) for configuration FTO/SnO$_2$/Cs$_2$PtI$_6$/MoO$_3$/C

Back Contact	Work function (ϕ)	V_{oc} (V)	J_{sc} (mA/cm^2)	FF (%)	PCE (%)
Cu [85]	4.53	0.72	26.822	67.60	13.14
Ni [86]	4.61	0.80	26.861	69.85	15.04
Ag [87]	4.74	0.92	26.905	73.11	18.14
Fe [88]	4.81	0.98	26.921	74.94	19.80
GO [89]	4.9	1.05	26.937	76.98	21.94
C [53]	5.0	1.12	26.949	78.08	23.52
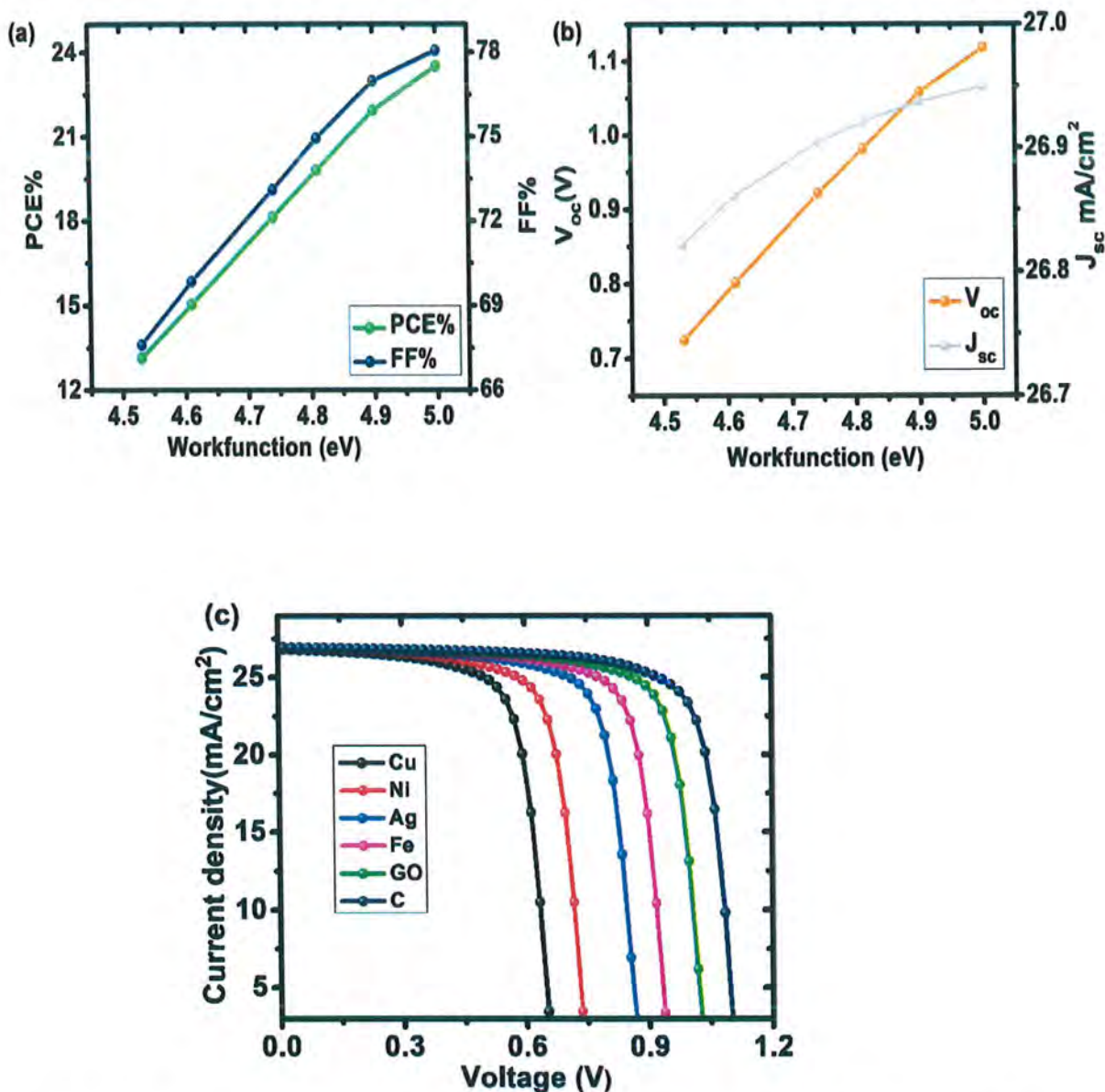
Figure 3.15: *Device performance as a function of back contact work function a) PCE and FF, b) V_{oc} and J_{sc}, c) J-V curve of device with different back contacts*

3.2.11 Comparison with the previous work

In comparison with the previously published data, this study demonstrates a significant advancement in solar cell efficiency. **Table 3.12** shows the performance comparison of this work and preceding work on Cs_2PtI_6 based perovskite solar cells. A remarkable improvement in power conversion efficiency is highlighted, showcasing the potential for further advancements in solar cell technology through the optimization strategies employed in this research.

Table 3.12: *Performance comparison of this work and preceding work on Cs_2PtI_6 based PSCs*

Device Architecture	V_{oc} (V)	J_{sc} (mA/cm^2)	FF (%)	PCE (%)	Experimental / Simulation	Reference
ITO/SnO$_2$/Cs$_2$PtI$_6$/ Spiro-OMeTAD /Au	0.73	1.20	82.00	0.72	Experimental	[50]
FTO/ CdS/ Cs$_2$PtI$_6$ with EDA/carbon/Cu	1.07	19.84	65.03	13.88	Experimental	[51]
FTO/CdS/Cs$_2$PtI$_6$/ Carbon/Cu	1.20	20.20	41.51	10.06	Experimental	[51]
FTO/ZnO/Cs$_2$PtI$_6$/ MoO$_3$/Cu	1.38	16.1070	75.54	16.85	Simulation	[53]
FTO/ZnO/Cs$_2$PtI$_6$/ MoO$_3$/C	1.41	16.1122	90.01	20.45	Simulation	[53]
FTO/CdS/Cs$_2$PtI$_6$/ MoO$_3$/Cu	1.11	20.14	61	13.9	Simulation	[54]
FTO/CdS/ Cs$_2$PtI$_6$/ Cu$_2$O /Cu	1.10	20.4	62	14.2	Simulation	[54]
FTO/CdS/ Cs$_2$PtI$_6$/ CuI /Cu	1.12	20.13	60	13.7	Simulation	[54]
FTO/IGZO/Cs$_2$PtI$_6$/ Cu$_2$O/C	1.13	22.2	59.2	14.8	Simulation	[54]
FTO/ZnSe/Cs$_2$PtI$_6$/ Cu$_2$O/C	1.12	22.3	58	14.7	Simulation	[54]
FTO/WS$_2$/Cs$_2$PtI$_6$/ Cu$_2$O/C	1.10	28.1	52.4	16.3	Simulation	[54]
FTO/SnO$_2$/Cs$_2$PtI$_6$/ MoO$_3$/GO	1.05	26.94	76.99	21.95	Simulation	This work
FTO/SnO$_2$/Cs$_2$PtI$_6$/ MoO$_3$/C	1.118	26.95	78.08	23.52	Simulation	This work

Conclusions

In this study, $Cs_2SnI_{6-x}Br_x$ films were successfully synthesized at temperatures 100 °C, 120 °C and 140 °C, and their properties were characterized using XRD (crystallinity), DRS (band gap), Hall measurements (electrical measurements), SEM (morphological studies) and EDX (elemental mapping) analyses. The investigation aimed to understand the influence of synthesis temperature on the structural, optical, and morphological properties of the films. It was observed that the synthesized films were crystalline, and with an increase in temperature, crystallite size decreased and band gap increased. Hall measurements revealed the material to be p-type, and best electrical properties were obtained at the highest temperature (140 °C). SEM analysis showed the change in morphology of $Cs_2SnI_{6-x}Br_x$ film compared to that of CsBr film, confirming the formation of perovskite but the morphology of film was irregular and needs further optimization. EDX mapping confirmed the presence of Cs, Sn, I and Br in the $Cs_2SnI_{6-x}Br_x$ perovskite film. Optical and electrical measurements revealed that the films could be used for solar cell application.

Using SCAPS-1D, design optimization of an ecologically friendly, lead-free Cs_2PtI_6 solar cell using MoO_3 as the HTL and SnO_2 as the ETL has been done. This research demonstrates that MoO_3 (HTL), Cs_2PtI_6, and SnO_2 (ETL) have a considerable effect on device performance. The impact of varying the defect densities of the interface and absorber layers demonstrated that these parameters are crucial for device performance and that fewer defects are necessary for improved device performance. It was determined that series resistance had little influence on V_{oc} but a substantial effect on PCE, FF, and J_{sc}. High R_{sh} and low R_s are needed for better device performance. In addition, the effect of temperature on the device functionality revealed that lower temperatures led to an improved performance. The spectral response of absorber material revealed that it was active. Cu, Ni, Ag, Fe, GO, and C were employed as back contacts, with work function of carbon (5.0 eV) being the best. The best performance was obtained with device architecture $FTO/SnO_2/Cs_2PtI_6/MoO_3/C$ with a PCE of 23.52 % (V_{oc} of 1.118 V, J_{sc} of 26.95 mA/cm^2, FF of 78.08 %).

References

1. Collins, W.; Colman, R.; Haywood, J.; Manning, M. R.; Mote, P., The physical science behind climate change. *Scientific American* **2007**, *297*(2), 64-73.

2. Panwar, N. L.; Kaushik, S. C.; Kothari, S., Role of renewable energy sources in environmental protection: a review. *Renewable and sustainable energy reviews* **2011**, *15*(3), 1513-1524.

3. Alrikabi, N., Renewable energy types. *Journal of Clean Energy Technologies* **2014**, *2*(1), 61-64.

4. Kangsabanik, J.; Sugathan, V.; Yadav, A.; Yella, A.; Alam, A., Double perovskites overtaking the single perovskites: a set of new solar harvesting materials with much higher stability and efficiency. *Physical Review Materials* **2018**, *2*(5), 055401.

5. Im, J. H.; Lee, C. R.; Lee, J. W.; Park, S. W.; Park, N. G., 6.5% efficient perovskite quantum-dot-sensitized solar cell. *Nanoscale* **2011**, *3*(10), 4088-4093.

6. Kim, J. Y.; Lee, J. W.; Jung, H. S.; Shin, H.; Park, N. G., High-efficiency perovskite solar cells. *Chemical Reviews* **2020**, *120*(15), 7867-7918.

7. Ball, J. M.; Lee, M. M.; Hey, A.; Snaith, H. J., Low-temperature processed meso-superstructured to thin-film perovskite solar cells. *Energy & Environmental Science* **2013**, *6*(6), 1739-1743.

8. Diau, E. W. G.; Jokar, E.; Rameez, M., Strategies to improve performance and stability for tin-based perovskite solar cells. *ACS Energy Letters* **2019**, *4*(8), 1930-1937.

9. Docampo, P.; Ball, J. M.; Darwich, M.; Eperon, G. E.; Snaith, H. J., Efficient organometal trihalide perovskite planar-heterojunction solar cells on flexible polymer substrates. *Nature communications* **2013**, *4*(1), 2761.

10. Min, H.; Lee, D. Y.; Kim, J.; Kim, G.; Lee, K. S.; Kim, J.; Paik, M. J.; Kim, Y. K.; Kim, K. S.; Kim, M. G.; Shin, T. J.; Il Seok, S., Perovskite solar cells with atomically coherent interlayers on SnO_2 electrodes. *Nature* **2021**, *598*(7881), 444-450.

11. Kojima, A.; Teshima, K.; Shirai, Y.; Miyasaka, T., Organometal halide perovskites as visible-light sensitizers for photovoltaic cells. *Journal of the American Chemical Society* **2009**, *131*(17), 6050-6051.

12. Juarez-Perez, E. J.; Hawash, Z.; Raga, S. R.; Ono, L. K.; Qi, Y., Thermal degradation of $CH_3NH_3PbI_3$ perovskite into NH_3 and CH_3I gases observed by coupled thermogravimetry–mass spectrometry analysis. *Energy & environmental science* **2016,** *9*(11), 3406-3410.

13. Juarez-Perez, E. J.; Ono, L. K.; Maeda, M.; Jiang, Y.; Hawash, Z.; Qi, Y., Photodecomposition and thermal decomposition in methylammonium halide lead perovskites and inferred design principles to increase photovoltaic device stability. *Journal of Materials Chemistry A* **2018,** *6*(20), 9604-9612.

14. Juarez-Perez, E. J.; Ono, L. K.; Qi, Y., Thermal degradation of formamidinium based lead halide perovskites into sym-triazine and hydrogen cyanide observed by coupled thermogravimetry-mass spectrometry analysis. *Journal of Materials Chemistry A* **2019,** *7*(28), 16912-16919.

15. Juarez-Perez, E. J.; Ono, L. K.; Uriarte, I.; Cocinero, E. J.; Qi, Y., Degradation mechanism and relative stability of methylammonium halide based perovskites analyzed on the basis of acid–base theory. *ACS applied materials & interfaces* **2019,** *11*(13), 12586-12593.

16. Ke, J. C. R.; Walton, A. S.; Lewis, D. J.; Tedstone, A.; O'Brien, P.; Thomas, A. G.; Flavell, W. R., In situ investigation of degradation at organometal halide perovskite surfaces by X-ray photoelectron spectroscopy at realistic water vapour pressure. *Chemical Communications* **2017,** *53*(37), 5231-5234.

17. Bryant, D.; Aristidou, N.; Pont, S.; Sanchez-Molina, I.; Chotchuangchutchaval, T.; Wheeler, S.; Durrant, J. R.; Haque, S. A., Light and oxygen induced degradation limits the operational stability of methylammonium lead triiodide perovskite solar cells. *Energy & Environmental Science* **2016,** *9*(5), 1655-1660.

18. Islam, M. B.; Yanagida, M.; Shirai, Y.; Nabetani, Y.; Miyano, K., Highly stable semi-transparent MAPbI$_3$ perovskite solar cells with operational output for 4000 h. *Solar Energy Materials and Solar Cells* **2019,** *195*, 323-329.

19. Jeng, J. Y.; Chen, K. C.; Chiang, T. Y.; Lin, P. Y.; Tsai, T. D.; Chang, Y. C.; Guo, T. F.; Chen, P.; Wen, T. C.; Hsu, Y. J., Nickel oxide electrode interlayer in $CH_3NH_3PbI_3$ perovskite/PCBM planar-heterojunction hybrid solar cells. *Advanced materials* **2014,** *26*(24), 4107-4113.

20. Jokar, E.; Chien, C. H.; Tsai, C. M.; Fathi, A.; Diau, E. W. G., Robust tin-based perovskite solar cells with hybrid organic cations to attain efficiency approaching 10 %. *Advanced materials* **2019,** *31*(2), 1804835.

21. Van Noorden, R., Cheap solar cells tempt businesses. *Nature News* **2014,** *513*(7519), 470.

22. Masi, S.; Gualdrón-Reyes, A. F.; Mora-Seró, I., Stabilization of black perovskite phase in FAPbI$_3$ and CsPbI$_3$. *ACS Energy Letters* **2020,** *5*(6), 1974-1985.

23. Burschka, J.; Pellet, N.; Moon, S. J.; Humphry-Baker, R.; Gao, P.; Nazeeruddin, M. K.; Grätzel, M., Sequential deposition as a route to high-performance perovskite-sensitized solar cells. *Nature* **2013,** *499*(7458), 316-319.

24. Kojima, A.; Teshima, K.; Shirai, Y.; Miyasaka, T., Organometal halide perovskites as visible-light sensitizers for photovoltaic cells. *Journal of the American Chemical Society* **2009,** *131*(17), 6050-6051.

25. Lee, M. M.; Teuscher, J.; Miyasaka, T.; Murakami, T. N.; Snaith, H. J., Efficient hybrid solar cells based on meso-superstructured organometal halide perovskites. *Science* **2012,** *338*(6107), 643-647.

26. Needleman, H., Lead poisoning. *Annual Review of Medicine* **2004,** *55,* 209-222.

27. Babayigit, A.; Ethirajan, A.; Muller, M.; Conings, B., Toxicity of organometal halide perovskite solar cells. *Nature materials* **2016,** *15*(3), 247-251.

28. Wang, M.; Wang, W.; Ma, B.; Shen, W.; Liu, L.; Cao, K.; Chen, S.; Huang, W., Lead-free perovskite materials for solar cells. *Nano-Micro Letters* **2021,** *13*(1), 62.

29. Ke, W.; Kanatzidis, M. G., Prospects for low-toxicity lead-free perovskite solar cells. *Nature communications* **2019,** *10*(1), 965.

30. Vargas, B.; Rodríguez-López, G.; Solis-Ibarra, D., The emergence of halide layered double perovskites. *ACS Energy Letters* **2020,** *5*(11), 3591-3608.

31. Cucco, B.; Katan, C.; Even, J.; Kepenekian, M.; Volonakis, G., Fine structure of excitons in vacancy-ordered halide double perovskites. *ACS Materials Letters* **2022,** *5*(1), 52-59.

32. Sa, R.; Zhang, Q.; Luo, B.; Liu, D., Exploring the electronic and optical properties of vacancy-ordered double perovskites Cs$_2$PtX$_6$ (X= Cl, Br, I). *Journal of Solid State Chemistry* **2021,** *304,* 122602.

33. Tian, C.; Huang, Q.; Wu, D.; Lai, J.; Qi, F.; Zhang, N.; Zhang, W.; Tang, X., Lead-free perovskite Cs$_2$XCl$_6$ (X = Hf, Zr, Te) microcrystals for photocatalytic CO$_2$ reduction. *Materials Today Energy* **2022,** *28,* 101067.

34. Dosi, A. T.; Rahayu, S.; Wulandari, P., Incorporation of perovskite Cs_2SnI_6 into dye sensitized solar cell structure and its optimization, *In Journal of Physics: Conference Series* **2022**, *2243*, 1, 012087, IOP Publishing.

35. Azad, A. K.; Eriksson, S. G.; Ivanov, S. A.; Mathieu, R.; Svedlindh, P.; Eriksen, J.; Rundlöf, H., Synthesis, structural and magnetic characterisation of the double perovskite A_2MnMoO_6 (A=Ba, Sr). *Journal of Alloys and Compounds* **2004**, *364*(1), 77-82.

36. Bartel, C. J.; Clary, J. M.; Sutton, C.; Vigil-Fowler, D.; Goldsmith, B. R.; Holder, A. M.; Musgrave, C. B., Inorganic halide double perovskites with optoelectronic properties modulated by sublattice mixing. *Journal of the American Chemical Society* **2020**, *142*(11), 5135-5145.

37. Lee, B.; Krenselewski, A.; Baik, S. I.; Seidman, D. N.; Chang, R. P., Solution processing of air-stable molecular semiconducting iodosalts, $Cs_2SnI_{6-x}Br_x$, for potential solar cell applications. *Sustainable Energy & Fuels* **2017**, *1*(4), 710-724.

38. Ullah, S.; Wang, J.; Yang, P.; Liu, L.; Khan, J.; Yang, S. E.; Xia, T.; Guo, H.; Chen, Y., Lead-free Cs_2SnI_6 perovskites for optoelectronic applications: recent developments and perspectives. *Solar RRL* **2021**, *5*(5), 2000830.

39. Han, X.; Liang, J.; Yang, J. H.; Soni, K.; Fang, Q.; Wang, W.; Zhang, J.; Jia, S.; Martí, A. A.; Zhao, Y., Lead-free double perovskite Cs_2SnX_6: facile solution synthesis and excellent stability. *Small* **2019**, *15*(39), 1901650.

40. Lee, B.; Stoumpos, C. C.; Zhou, N.; Hao, F.; Malliakas, C.; Yeh, C. Y.; Marks, T. J.; Kanatzidis, M. G.; Chang, R. P., Air-stable molecular semiconducting iodosalts for solar cell applications: Cs_2SnI_6 as a hole conductor. *Journal of the American Chemical Society* **2014**, *136*(43), 15379-15385.

41. Qiu, X.; Jiang, Y.; Zhang, H.; Qiu, Z.; Yuan, S.; Wang, P.; Cao, B., Lead-free mesoscopic Cs_2SnI_6 perovskite solar cells using different nanostructured ZnO nanorods as electron transport layers. *physica status solidi (RRL)–Rapid Research Letters* **2016**, *10*(8), 587-591.

42. Kaltzoglou, A.; Antoniadou, M.; Kontos, A. G.; Stoumpos, C. C.; Perganti, D.; Siranidi, E.; Raptis, V.; Trohidou, K.; Psycharis, V.; Kanatzidis, M. G., Optical-vibrational properties of the Cs_2SnX_6 (X= Cl, Br, I) defect perovskites and hole-transport efficiency in dye-sensitized solar cells. *The Journal of Physical Chemistry C* **2016**, *120*(22), 11777-11785.

43. Kaltzoglou, A.; Perganti, D.; Antoniadou, M.; Kontos, A. G.; Falaras, P., Stress tests on dye-sensitized solar cells with the Cs_2SnI_6 defect perovskite as hole-transporting material. *Energy Procedia* **2016**, *102*, 49-55.

44. Qiu, X.; Cao, B.; Yuan, S.; Chen, X.; Qiu, Z.; Jiang, Y.; Ye, Q.; Wang, H.; Zeng, H.; Liu, J., From unstable $CsSnI_3$ to air-stable Cs_2SnI_6: A lead-free perovskite solar cell light absorber with bandgap of 1.48 eV and high absorption coefficient. *Solar Energy Materials and Solar Cells* **2017**, *159*, 227-234.

45. Pujiarti, H.; Hidayat, R.; Wulandari, P. Effect of lead-free perovskite Cs_2SnI_6 addition in the structure of dye-sensitized solar cell, In *Key Engineering Materials* **2020**, *860*, 22-27, Trans Tech Publications Ltd.

46. Qamar, S.; Sultan, M.; Akhter, Z.; Ela, S. E., A facile one-step solution synthesis of $Cs_2SnI_{6-x}Br_x$ using less-toxic methanol solvent for application in dye-sensitized solar cells. *International Journal of Energy Research* **2022**, *46* (10), 13441-13452.

47. Zhang, G.; Zhang, J.; Liao, Y.; Pan, Z.; Rao, H.; Zhong, X., Cs_2SnI_6 nanocrystals enhancing hole extraction for efficient carbon-based $CsPbI_2Br$ perovskite solar cells. *Chemical Engineering Journal* **2022**, 440, 135710.

48. Wang, J.; Ullah, S.; Yang, P.; Liu, L.; Yang, S.; Xia, T.; Guo, H.; Chen, Y., A feasible process for lead-free Cs_2SnI_6 films using vapor-assisted deposition method with Sn and I_2 powders as reactants. *Journal of Physics D Applied Physics* **2021**, *54*(14), 145101.

49. Ullah, S.; Ullah, S.; Wang, J.; Yang, S.-E.; Xia, T.; Guo, H.; Chen, Y., Investigation of air-stable Cs_2SnI_6 films prepared by the modified two-step process for lead-free perovskite solar cells. *Semiconductor Science and Technology* **2020**, *35*(12), 125027.

50. Schwartz, D.; Murshed, R.; Larson, H.; Usprung, B.; Soltanmohamad, S.; Pandey, R.; Barnard, E. S.; Rockett, A.; Hartmann, T.; Castelli, I. E., Air stable, high-efficiency, Pt-based halide perovskite solar cells with long carrier lifetimes. *physica status solidi (RRL)–Rapid Research Letters* **2020**, *14*(8), 2000182.

51. Yang, S.; Wang, L.; Zhao, S.; Liu, A.; Zhou, Y.; Han, Q.; Yu, F.; Gao, L.; Zhang, C.; Ma, T., Novel lead-free material Cs_2PtI_6 with narrow bandgap and ultra-stability for its photovoltaic application. *ACS Applied Materials & Interfaces* **2020**, *12*(40), 44700-44709.

52. Hamdan, M.; Chandiran, A. K., Cs_2PtI_6 halide perovskite is stable to air, moisture, and extreme pH: application to photoelectrochemical solar water oxidation. *Angewandte Chemie* **2020,** *132*(37), 16167-16172.

53. Shamna, M.; Sudheer, K., Device modeling of Cs_2PtI_6-based perovskite solar cell with diverse transport materials and contact metal electrodes: a comprehensive simulation study using solar cell capacitance simulator. *Journal of Photonics for Energy* **2022,** *12*(3), 032211.

54. AbdElAziz, H. H.; Taha, M.; El Rouby, W. M.; Khedr, M.; Saad, L., Evaluating the performance of $Cs_2PtI_{6-x}Br_x$ for photovoltaic and photocatalytic applications using first-principles study and SCAPS-1D simulation. *Heliyon* **2022,** *8*(10), e10808.

55. Abass, A., Light absorption enhancement and electronic properties of thin-film solar cells. Doctoral dissertation, Ghent University, **2014.**

56. Manser, J. S.; Christians, J. A.; Kamat, P. V., Intriguing optoelectronic properties of metal halide perovskites. *Chemical Reviews* **2016,** *116*(21), 12956-13008.

57. Tai, Q.; Tang, K. C.; Yan, F., Recent progress of inorganic perovskite solar cells. *Energy & Environmental Science* **2019,** *12*(8), 2375-2405.

58. Wang, X.; Wang, Y.; Chen, Y.; Liu, X.; Zhao, Y., Efficient and stable $CsPbI_3$ inorganic perovskite photovoltaics enabled by crystal secondary growth. *Advanced Materials* **2021,** *33*(44), 2103688.

59. You, J.; Meng, L.; Song, T. B.; Guo, T. F.; Yang, Y. M.; Chang, W. H.; Hong, Z.; Chen, H.; Zhou, H.; Chen, Q., Improved air stability of perovskite solar cells via solution-processed metal oxide transport layers. *Nature nanotechnology* **2016,** *11*(1), 75-81.

60. Nawaz, A., Perovskite solar cells: improved active layer morphology and pore-filling in TiO_2 nano-scaffolds. Doctoral thesis, University of South-Eastern Norway, **2018.**

61. Cui, X. P.; Jiang, K. J.; Huang, J. H.; Zhang, Q. Q.; Su, M. J.; Yang, L. M.; Song, Y. L.; Zhou, X. Q. J. S. M., Cupric bromide hybrid perovskite heterojunction solar cells. *Synthetic metals* **2015,** *209*, 247-250.

62. Marinova, N.; Valero, S.; Delgado, J. L., Organic and perovskite solar cells: working principles, materials and interfaces. *Journal of colloid and interface science* **2017,** *488*, 373-389.

63. Murugan, P.; Hu, T.; Hu, X.; Chen, Y., Current development toward commercialization of metal-halide perovskite photovoltaics. *Advanced Optical Materials* **2021**, *9*(17), 2100390.

64. Ahmad, O.; Rashid, A.; Ahmed, M. W.; Nasir, M. F.; Qasim, I., Performance evaluation of Au/p-CdTe/Cs_2TiI_6/n-TiO_2/ITO solar cell using SCAPS-1D. *Optical Materials* **2021**, *117*, 111105.

65. Ahmed, S.; Jannat, F.; Khan, M. A. K.; Alim, M. A., Numerical development of eco-friendly Cs_2TiBr_6 based perovskite solar cell with all-inorganic charge transport materials via SCAPS-1D. *Optik* **2021**, *225*, 165765.

66. Sochi, T. (2010)., High throughput software for powder diffraction and its application to heterogeneous catalysis. *arXiv preprint arXiv* **2010**, *101*, 4506.

67. Rades, S.; Hodoroaba, V. D.; Salge, T.; Wirth, T.; Lobera, M. P.; Labrador, R. H.; Natte, K.; Behnke, T.; Gross, T.; Unger, W. E., High-resolution imaging with SEM/T-SEM, EDX and SAM as a combined methodical approach for morphological and elemental analyses of single engineered nanoparticles. *RSC advances* **2014**, *4*(91), 49577-49587.

68. Kortüm, G.; Braun, W.; Herzog, G., Principles and techniques of diffuse-reflectance spectroscopy. *Angewandte Chemie International Edition in English* **1963**, *2*(7), 333-341.

69. Cubas, J.; Pindado, S.; De Manuel, C., Explicit expressions for solar panel equivalent circuit parameters based on analytical formulation and the Lambert W-function. *Energies* **2014**, *7*(7), 4098-4115.

70. Hanmin, T.; Xiaobo, Z.; Shikui, Y.; Xiangyan, W.; Zhipeng, T.; Bin, L.; Ying, W.; Tao, Y.; Zhigang, Z., An improved method to estimate the equivalent circuit parameters in DSSCs. *Solar Energy* **2009**, *83*(5), 715-720.

71. Kyaw, H. H.; Bora, T.; Dutta, J., One-diode model equivalent circuit analysis for ZnO nanorod-based dye-sensitized solar cells: effects of annealing and active area. *IEEE transactions on nanotechnology* **2012**, *11*(4), 763-768.

72. Mashreghi, A.; Moghadam, F. B., Effect of photoanode active area on photovoltaic parameters of dye sensitized solar cells through its effect on series resistance investigated by electrochemical impedance spectroscopy. *Journal of Solid State Electrochemistry* **2016**, *20*(5), 1361-1368.

73. Yoder, C. S.; Shenk, S.; Schaeffer, R. W.; Chan, B.; Molinaro, M.; Morissey, S.; Yoder, C. H., The synthesis, characterization, and lewis acidity of SnI_2 and SnI_4. *Journal of Chemical Education* **1997**, *74*(5), 575.

74. Karimi, E.; Ghorashi, S., Investigation of the influence of different hole-transporting materials on the performance of perovskite solar cells. *Optik* **2017**, *130*, 650-658.

75. Lakhdar, N.; Hima, A., Electron transport material effect on performance of perovskite solar cells based on $CH_3NH_3GeI_3$. *Optical Materials* **2020**, *99*, 109517.

76. Li, W.; Li, W.; Feng, Y.; Yang, C., Numerical analysis of the back interface for high efficiency wide band gap chalcopyrite solar cells. *Solar Energy* **2019**, *180*, 207-215.

77. Amjad, A.; Qamar, S.; Zhao, C.; Fatima, K.; Sultan, M.; Akhter, Z., Numerical simulation of lead-free vacancy ordered Cs_2PtI_6 based perovskite solar cell using SCAPS-1D. *RSC advances* **2023**, *13*(33), 23211-23222.

78. Lin, L.; Jiang, L.; Li, P.; Qiu, Y.; Yan, Q., Numerical analysis of inverted-structure perovskite solar cell based on all-inorganic charge transport layers. *Journal of Photonics for Energy* **2019**, *9*(2), 024501-024501.

79. Tan, K.; Lin, P.; Wang, G.; Liu, Y.; Xu, Z.; Lin, Y., Controllable design of solid-state perovskite solar cells by SCAPS device simulation. *Solid-State Electronics* **2016**, *126*, 75-80.

80. Ahmed, S.; Harris, J.; Shaffer, J.; Devgun, M.; Chowdhury, S.; Abdullah, A.; Banerjee, S., Simulation studies of Sn-based perovskites with Cu back-contact for non-toxic and non-corrosive devices. *Journal of Materials Research* **2019**, *34*, 2789-2795.

81. Hagfeldt, A.; Boschloo, G.; Sun, L.; Kloo, L.; Pettersson, H., Dye-sensitized solar cells. *Chemical reviews* **2010**, *110*(11), 6595-6663.

82. Hossain, S.; Amin, N.; Martin, M.; Aliyu, M. M.; Razykov, T.; Sopian, K., A numerical study on the prospects of high efficiency ultra thin $Zn_xCd_{1-x}S/CdTe$ solar cell. *Chalcogenide letters* **2011**, *8*(4).

83. Chakraborty, K.; Choudhury, M. G.; Paul, S., Numerical study of Cs_2TiX_6 (X= Br^-, I^-, F^- and Cl^-) based perovskite solar cell using SCAPS-1D device simulation. *Solar Energy* **2019**, *194*, 886-892.

84. Fahrenbruch, A.; Bube, R., Fundamentals of solar cells: photovoltaic solar energy conversion. *Elsevier*, **2012**.

85. Zangmeister, C. D.; Picraux, L. B.; van Zee, R. D.; Yao, Y.; Tour, J. M., Energy-level alignment and work function shifts for thiol-bound monolayers of conjugated molecules self-assembled on Ag, Cu, Au, and Pt. *Chemical physics* **2007**, *442*(4-6), 390-393.

86. Sachtler, W.; Dorgelo, G., The surface of copper-nickel alloy films: I. Work function and phase composition. *Journal of Catalysis* **1965**, *4*(6), 654-664.

87. Dweydari, A.; Mee, C., Work function measurements on (100) and (110) surfaces of silver. *physica status solidi (a)* **1975**, *27*(1), 223-230.

88. Wu, R.; Freeman, A., Structural, electronic, and magnetic properties of an open surface: Fe (111). *Physical Review B* **1993**, *47*(7), 3904.

89. Jayaraman, J. P.; Hamdan, M.; Velpula, M.; Kaisare, N. S.; Chandiran, A. K., $BiVO_4/Cs_2PtI_6$ vacancy-ordered halide perovskite heterojunction for panchromatic light harvesting and enhanced charge separation in photoelectrochemical water oxidation. *ACS Applied Materials & Interfaces* **2021**, *13*(14), 16267-16278.